Journal of The Electrochemical Society

Morphological Evolution and Dealloying During Corrosion of Ni20Cr (wt.%) in Molten FLiNaK Salts

To cite this article: Ho Lun Chan *et al* 2024 *J. Electrochem. Soc.* **171** 081501

Journal of The Electrochemical Society, 2024 **171** 081501

Morphological Evolution and Dealloying During Corrosion of Ni20Cr (wt.%) in Molten FLiNaK Salts

Ho Lun Chan,[1,2,z,*] Elena Romanovskaia,[1,2,] Sean H. Mills,[3,4] Minsung Hong,[5,6] Valentin Romanovski,[1,2] Nathan Bieberdorf,[3] Chaitanya Peddeti,[3] Andrew M. Minor,[3,4] Peter Hosemann,[5,7] Mark Asta,[3] and John R. Scully[1,2,**,z]**

[1]*Department of Materials Science and Engineering, University of Virginia, Charlottesville, Virginia 22904, United States of America*
[2]*Center for Electrochemical Science and Engineering, University of Virginia, Charlottesville, Virginia 22904, United States of America*
[3]*Department of Materials Science and Engineering, University of California, Berkeley, California 94720, United States of America*
[4]*National Center for Electron Microscopy, Molecular Foundry, Lawrence Berkeley National Laboratory, Berkeley, California 94720, United States of America*
[5]*Department of Nuclear Engineering, University of California, Berkeley, California 94150, United States of America*
[6]*Materials Safety Technology Research Division, Korea Atomic Energy Research Institute, Daejeon, 34057, Republic of Korea*
[7]*Materials Science Division, Lawrence Berkeley National Laboratory, Berkeley, California 94720, United States of America*

The dealloying corrosion behavior of the FCC Ni20Cr (wt%) in molten LiF-NaF-KF (FLiNaK) salts at 600 °C under varying applied potentials was investigated. Using *in-operando* electrochemical techniques and a multi-modal suite of characterization methods, we connect electrochemical potential, thermodynamic stability, and electro-dissolution kinetics to the corrosion morphologies. Notably, under certain potential regimes, a micron-scale bicontinuous structure, characterized by a network of interconnected pores and ligaments riched with the composition of the more noble (MN) element, becomes prominent. At other potentials both MN and less noble (LN) elements dealloy but at different rates. The dealloying process consists of lattice and grain boundary diffusion of Cr to the metal/salt interface, interphase Cr oxidation, accompanied by surface diffusion of Ni to form interconnected ligaments. At higher potentials, the bicontinuous porous structure undergoes further surface coarsening. Concurrently, Cr(II), Cr(III), and Ni(II) begin to dissolve, with the dissolution of Ni occurring at a significantly slower rate. When solid-state transport of Cr is exceeded by the interfacial rates, dealloying depths are limited.
 [DOI: 10.1149/1945-7111/ad6037]

Manuscript submitted March 19, 2024; revised manuscript received May 24, 2024. Published August 5, 2024.

Supplementary material for this article is available online

Molten salt reactor (MSR), whether in modular or industrial-scale configuration, is on the cusp of commercial deployment, representing a substantial step forward in the evolution of next-generation nuclear power systems. In essence, MSR employs a molten chloride or fluoride salt blend for nuclear power generation and energy storage applications.[1] The corrosion protection of structural alloys in these applications necessitates resistance both to molten salt corrosion for salt-facing materials and to air oxidation for external surfaces.[2–5] Ni-based superalloys and stainless steels (304 and 316) are often considered for use in structural applications in hot water reactors and MSR. However, Cr(II)-O and Cr(III)-O species are not as thermodynamically stable as Cr(II)-F and Cr(III)-F species, such as CrF_2, CrF_3, CrF_3^- or CrF_6^{3-}.[6] The unavoidable presence of oxidizing impurities, such as moisture-induced hydrofluoric acid (HF) and chromium cations (Cr(III)),[7,8] induce a potential-dependent thermodynamic driving force to dissolve LN from the alloy.

One example is the corrosion of NiCr alloys in molten fluorides.[6,7,9,10] In this system, the dissolution of Cr and Ni from the alloy can occur via reactions (1) and (2) to their stable fluoride forms. The notation "MS" represents the ionic molten salt phase. In molten fluorides, Cr is the LN and Ni is the MN[2]. The LN can leach from the alloy preferentially through short-circuit diffusion pathways, such as grain boundaries.[11,12] The driving force for (1) and (2) is described in terms of their half-cell redox potentials (E_{redox}) and can be manipulated through chemical or electrochemical methods.

$$Cr\ (s) + 3F^-(MS) \rightarrow CrF_3^-\ (MS) + 2e^- \quad [1]$$

$$Ni\ (s) + 2F^-(MS) \rightarrow NiF_2\ (MS) + 2e^- \quad [2]$$

To introduce a controlled concentration, or activity, an oxidizer with a higher reduction power than (1) and (2), such as HF/H_2 (reaction 3) and EuF_3/EuF_2 (reaction 4) can be added to the salt.[13,14] The coupled anodic and cathodic reactions thermodynamically and kinetically establish the corrosion potential (E_{corr}), which is a mixed potential under open-circuit conditions. An earlier work by the authors has tabulated and compared a range of possible half-cell redox reactions suitable for identifying LN and MN elementsin an alloy as well as oxidizing species, such as HF and EuF_3, that may drive spontaneous corrosion.[9] However, controlling the activity of an oxidant *in-situ* during a corrosion experiment is challenging as it is being continuously consumed during exposure[7] and difficult to maintain in a large and complicated system where several other factors need to be balanced. Some other approaches include changing temperature[15] and applying a precise electrochemical potential relative to the thermodynamic phase stability of the salt system.[6,9] Through these approaches, electrode potential can be regulated to enable selective dealloying of Cr (i.e., $E_{redox}^{Cr/LN} < E_{Corr}^{Alloy} < E_{redox}^{Ni/MN}$) or simultaneous dissolution of both Ni and Cr (i.e., $E_{Corr}^{Alloy} > E_{redox}^{Cr/LN}$ *and* $E_{redox}^{Ni/MN}$).

$$HF\ (MS) + e^- \rightarrow \frac{1}{2}H_2\ (g) + F^-(MS) \quad [3]$$

$$EuF_3\ (MS) + e^- \rightarrow EuF_2\ (MS) + F^-(MS) \quad [4]$$

The selective dealloying of Cr in NiCr alloys results in Ni enrichment on the surface, which undergoes surface diffusion, collection and coarsening of surface features, leading to the

*Electrochemical Society Student Member.
**Electrochemical Society Member.
***Electrochemical Society Fellow.
[z]E-mail: hc4ry@virginia.edu; jrs8d@virginia.edu

formation of a micron-scale bicontinuous porous structure.[15–21] The phenomenon of dealloying corrosion is of particular concern as the dealloyed layer can become vulnerable to stress corrosion cracking[22] and/or hot spot formation [13] during heat transfer that endangers the Gen-IV reactor application. The phenomenon of dealloying corrosion has garnered considerable interest, particularly due to its prevalence at high homologous temperatures. A high homologous temperature (T_H: 0.3–0.5) is within the practical service temperature range of the MSR between 500 °C and 900 °C.[23], whererapid bulk solid-state diffusion of LN element can become the rate-limiting mechanism for corrosion dealloying. The multiple solid-state diffusion processes include LN element outward bulk lattice diffusion, short-circuit diffusion via grain boundaries and dislocation pipes or accelerated by radiation-induced defects,[24] MN element surface diffusion which uncovers unreacted Cr in underlying layers, and long-range ionic diffusion of dissolved metal cations or oxidizers, influenced by the solubility and fluid dynamics of the molten salts.[16,25–27] The bulk diffusion-assisted dealloyingis observed to reduce the parting limit of dealloying in binary NiCr and FeCr alloys to approximately 20 at% of the LN in molten salts,[16,25–27] a sharp contrast to the 50–60 at% typical in RT aqueous solutions.[22] In contrast, at lower T_H such as during Ag-Au dealloying at room temperature, the LN bulk diffusion (Ag in this case) becomes negligible relative to its rate of oxidation. A LN element concentration limit to enable a connected silver path with Ag essentially frozen in place can be defined by a percolation or advanced percolation processes[28]. The implication of bulk diffusion-assisted dealloying is that the corrosion process is now governed by a myriad of factors at different length scales that introduces further variability to the corrosion morphology,[29] including grain size, point defect-solute interaction[30,31] and electrochemical potential.[25] For instance, if the grain boundary diffusion of LN element is much faster than bulk lattice diffusion (e.g. due to finer grain size[27]), severe grain boundary corrosion can be anticipated. Within the grain surface, the surface diffusion of MN element occurs simultaneously with LN oxidation and bulk diffusion, leading to the formation of a a three-dimensional, bicontinuous porous morphology.

In a collection of investigations led by Chen-Wiegart et al.,[16–18,32,33] using *in-situ* synchrotron X-ray nano-tomography, the authors observed the formation of bicontinuous porous structure on Ni20Cr (wt%) microwires and thin foils at both nano and micron scale when statically exposed to molten chlorides (e.g. KCl–$MgCl_2$) between 500 °C and 800 °C. The dealloying process in their cases relied on moisture and other impurities as oxidizers to drive the Cr dealloying process.[16–18,32,33] The electrode potential of the NiCr was not controlled. More recently, Ghaznavi, Persaud, and Newman[15,19,20] employed a single potentiostatic hold approach applying a small overpotential of 30 to 100 mV to prompt the dealloying of Cr in molten LiCl-KCl and LiCl-KCl-$MgCl_2$ from Fe52Ni48 (at%), Fe30Cr22Ni48 (at%), Ni78Cr22 (at%), and other model alloys between 350 °C and 700 °C. Specifically, the authors elaborate on the bicontinuous dealloying process mechanism relative to the effects of temperature,[15] alloy composition,[20] and crystallographic orientation. Both authors recognize the role of bulk diffusion at high T_H in dealloying.[15–20]

While both methodologies offer numerous advantages, challenges in controlling corrosion-driving forces persist. This aspect is critical as the process is highly dependent on the condition of $E^{Cr/\,LN}_{Nernst} < E^{Alloy} < E^{Ni/MN}_{redox}$, where it is commonly assumed that only LNdissolves, although in certain instances, both elements may dissolve. In many instances of impurity-driven corrosion, the depletion of impurities and accumulation of dissolved corrosion products can alter the driving force for half-cell cathodic reactions (according to the Nernst equation) as a function of exposure time, though this behavior is difficult to predict.[7]

A fundamental knowledge gap exists in systematically considering tight control of electrode potential that alters the corrosion morphology. This issue is multi-faceted at high T_H, owing to the vast combination of possible influencing factors, including but not limited to temperature,[15,32] composition,[20,34,35] time,[16,36,37] microstructural properties (such as grain size and grain orientation),[26,27,31,38] and salt impurities.[14,39] The corrosion potential determines which alloying species are thermodynamically favorable to dissolve as well as their rates during activation-controlled electrolytic dissolution [2]. Critically, the primary mechanism limiting dealloying may shift during this potential-dependent dissolution process. For example, initial fully activation-controlled dissolution of Cr can lead to Ni surface enrichment, which then serves as a barrier to slow down the bulk diffusion of Cr,[40] and may change the primary rate-limiting mechanism from interfacial reaction-control to Ni surface diffusion or bulk diffusion regulated mass transport-controlled.[15] Another scenario that requires further investigation is whether a bicontinuous structure will still form in a molten salt medium if both Ni and Cr dissolve under sufficient driving force. There is a need for comprehensive studies correlating variations in applied electrochemical potential with the thermodynamic regions for stability of selected soluble metal salt species and the associated alloy dissolution kinetics.[6,9] Our previous work, which investigated the corrosion behavior of pure Cr in molten FLiNaK,[25] demonstrated that Cr can exhibit a diverse range of potential dependent corrosion morphologies—from micro-porosity to surface faceting to salt-film induced smoothing –depending on the applied potential. Extending this approach, the present study explores the morphological evolution of Ni20Cr in FLiNaK under various applied potentials that enable dealloying.

This work aims to study the morphological evolution of Ni20Cr in molten FLiNaK salts at 600 °C due to various applied potentials where preferential dissolution and dealloying occur. By modulating the applied potential, the corrosion behavior of Ni20Cr experiencing various controlled driving forces can be investigated. The objective is to pinpoint the potential effects and mechanisms responsible for morphologies such as bicontinuous dealloying, as well as identify the governing thermodynamic and kinetic regimes.

Materials and Methods

Materials preparation.—Ni20Cr alloys (80 wt%Ni-20 wt%Cr) were prepared by mixing high purity Ni (99.98%, Thermo Scientific) and Cr (99.99%, Thermo Scientific) at a desired stochiometric ratio, then subjecting the alloys to a vacuum arc-melting process ($>10^{-5}$ torr). The Ni20Cr alloys were re-melted three times to ensure a homogenous composition. Additionally, the Ni20Cr alloys were also solution homogenized at 1050 °C for 6 h in an encapsulated Ar-filled quartz tube and were then quenched in room temperature water. The as-homogenized Ni20Cr alloy was a random solid solution that exhibits an average grain size of 351 ± 154 μm. The Ni20Cr samples were then machined to a rectangular plate with the dimension of 2 ± 0.5 × 1 ± 0.5 × 0.5 ± 0.3 cm, polished to 1200 grit surface finish using silicon carbide paper, and lastly sonicated in deionized water (18.2 Ω·cm^2) and isopropanol for 3 min prior to experimentation. Baseline microstructural characterization was carried out on fabricated Ni20Cr samples and can be seen in Fig. S1.

Salt preparation.—The LiF-NaF-KF (46.5–11.5–42 mol%) eutectic salt (FLiNaK) is selected as the salt electrolyte. Fluoride salt constituents, including LiF (99.99% purity, Fisher Scientific), 11.5 mol% NaF (99.99% purity, Fisher Scientific), and 42 mol% KF (>99.5% purity, Fisher Scientific) salts, were obtained from commercial vendors, dried in a vacuum oven at 100 °C for 48 h, transferred to an N_2-filled (with oxygen and H_2O controlled below <0.1 ppm) glove box (UNIlab MBraun, USA), and mixed into their targeted stoichiometric ratio. 30 g of FLiNaK salt was used for each test. This study employs a two-step drying process. The salt mixture was first heated to 600 °C under the flow of ultra-high purity (UHP) N_2 gas with 99.999% purity for a minimum of 6 h. This was done to ensure the removal of any trapped oxygen and moisture. After

cooling and solidifying, the salt mixture was reheated to the target temperature and maintained for 3 h before the electrochemical experiment. No additional purification steps (e.g. HF purging[39]) were performed to enable the removal of all metallic cations, O_2, or moisture. Thus, the salt may be considered as unpurified. Nevertheless, our recent work focusing on the validation of molten salt electrochemistry[25] reveals that during anodic polarization on the working electrode (the main focus of this study), impurities such as metallic cations, moisture, and molten K^+ ions can be consumed by reduction at the counter electrode to support the ionic current flow. This phenomenon merely suggests that the driving force of Cr/Cr (III) and/or Ni/Ni(II) reactions responsible for Ni20Cr dealloying is supported by the potentiostat instead of relying on the oxidizing impurities (e.g. HF/H_2). While the effect of impurities may still be present during an anodic polarization scan, this has not been investigated in the current study and will be addressed in future work.

Molten salt electrochemistry experiments.—The electrochemical experiments were conducted in a 4-electrodes cell in a glove box environment. Schematics and additional details on the electrochemical cell configuration as well as electrode design are outlined in our earlier work.[7] A high purity boron nitride crucible (>99.6%, MSE Supplies) was utilized as the salt container. A graphite rod (0.25 inch in diameter) was used as the counter electrode (CE) and a high purity 5 mm diameter Pt wire (99.95%, Fisher Scientific) as the pseudo-reference electrode. Two working electrodes (WE) were employed in this work. The primary WE was the Ni20Cr sample, on the end of which a Ni20Cr wire (99.99%, Fisher Scientific) was spot-welded. This wire was threaded through an alumina tube, and the welded spot was covered with boron nitride paste. The secondary WE was another high purity Pt wire (99.95%, Fisher Scientific). It is noted that no gas flow was maintained during the electrochemistry experiments.

Prior to testing the Ni20Cr samples, cyclic voltammetry (CV) experiment was performed at 100 mV s^{-1} in the potential range from 0 V_{Pt} to -2.0 ± 0.3 V_{Pt} to identify the equilibrium K^+/K potential as well as any redox reactions that may suggest the presence of metallic cation impurities within the potential range (Fig. S2).[6,7,25,41,42] It is noted, however, that the K^+/K electron transfer kinetics are significantly faster than the typical range of scan rates utilized in CV experiments (up to 500 mV s^{-1}),[6] and therefore the effect of scan rate on the equilibrium K^+/K potential value is minimal (see Fig. S2). It is noted that the K^+/K potential can also be obtained by a dynamic reference electrode (DRE) method in which the pseudo reference electrode is cathodically polarized;[19,25,41] however, F_2 bubble evolution may occur from F^- oxidation that adds infinite resistance to disrupt the polarization experiments.[25] In this work, the equilibrium K^+/K potential was determined immediately prior to the electrochemical scan on a Pt wire. The K^+/K potential measurement was performed during the experiment to ensure the continuous verification and/or calibration of the applied potential in relation to the established K^+/K potential.

In this study, three sets of electrochemical experiments were conducted. Each experiment was performed in triplicate to ensure replicability:

Experiment #1: Ni20Cr alloys were subjected to a 60 s open-circuit potential (E_{oc}) measurement coupled with linear sweep voltammetry (LSV) (or potentiodynamic polarization) at 1 mV/s from −0.4 V to +1.5 V vs. E_{oc}. The 60 s period was deemed enough time to dissolve oxides based on previous work.[43] The fast scan rate precludes significant dissolution. The same scan was also conducted on pure Ni and Cr for baseline comparison. Electrochemical thermodynamic calculations were performed following previously established methods[2,6,9,42] to relate the potential regimes to the phase stability of Cr, Ni, Ni(II), Cr(II), and Cr (III) species in molten FLiNaK. Additionally, the anodic polarization portion of the E-log(*i*) result was also corrected with iR drop and for the presence of cathodic current densities.[25,44]

Experiment #2: Potentiostatic polarization was carried out on Ni20Cr samples at applied potentials ($E_{applied}$) over a 1 V range from +1.75, +1.90, +2.10, +2.30, +2.50, to +2.75 $V_{K+/K}$ for 10 ks (see section 3.1 for the choice of $E_{applied}$). During each 1 ks interval, electrochemical impedance spectroscopy (EIS) was performed on the samples at the specified $E_{applied}$, spanning a frequency domain from 10 kHz to 10 mHz, with an AC perturbation of 20 mV. An electrical equivalent circuit (EEC) model was used in an attempt to calculate the interfacial charge-transfer resistance (R_{ct}). Simultaneously, CV scans were also performed on the secondary WE Pt wire at each 1 ks interval with a scan rate of 100 mV s^{-1} to identify the presence of dissolved Cr(II), Cr(III), and Ni(II) species remote from the Ni20Cr electrode. Additionally, to estimate the dissolved NiCr depth of attack ($h_{dissolved}$) neglecting porosity during the potentiostatic hold, Faraday's Law of mass and charge conversion was utilized, as outlined in Eq. 5:[7,25]

$$h_{dissolved} = \frac{EW \cdot i_{electric} \cdot t}{F \cdot \rho} \quad [5]$$

where $i_{electric}$ is measured current density in A cm^{-2}, t is time in seconds, F is the Faraday constant of 96500 C mol^{-1}, ρ is the density in g cm^{-3}, and EW is the equivalent weight (EW). The method of determining EW can be found in the ASTM G102–89 standard via Eq. 6:[45]

$$EW = \sum \frac{W_i}{n_i f_i} \quad [6]$$

where W_i represents the atomic weight, n_i is the oxidation state, and f_i is the weight fraction of the i^{th} alloying elements. Note the dissolution flux (J_e) was also calculated in terms of $i_{.e.}$ via $J_e = i_{.e.}/nF$.

Experiment #3: *Experiment #2* was replicated on Ni20Cr alloys in FLiNaK with 1 wt% NiF_2 addition (97 wt%, Alfa Aesar) at the $E_{applied}$ of +1.90 and +2.10 $V_{K+/K}$ for 10 ks. A series of CV diagnostics was performed on a Pt wire in FLiNaK with the addition of 0.05 wt% to 1.00 wt% NiF_2 to approximate the half-cell redox potential of the Ni/Ni(II) reaction in molten FLiNaK at 600 °C as shown in Fig. S3.

Scanning electron microscopy (SEM) and energy dispersive spectroscopy (EDS).—Both the surface and cross-section of the corroded Ni20Cr samples were examined using a FEI Quanta 3D FEG scanning electron microscopy (SEM) equipped with an Oxford Energy Dispersive Spectroscopy (EDS). Upon experiments, the electrodes were removed immediately from the salt bath and N_2 cooled in the glove box. The samples were then sonicated in deionized H_2O until visible residual salts on the surface were removed. Upon surface SEM analysis, the corroded Ni20Cr coupons were sectioned and mechanically polished sequentially from 400 to 1200 grit using SiC metallography pads, and finally polished via a vibratory polisher in a 0.5 μm colloidal SiO_2 polishing suspension. This paper focused on the planar dealloying front.

Electron backscattered scattered diffraction (EBSD).—Electron Backscatter Diffraction (EBSD) (Thermo Fisher Scientific, Scios 2, field emission gun SEM) was performed to observe the selective dissolution along the grain boundaries. The specimen was polished to 0.05 μm using an alumina suspension and at sonicated for 10 min in ethanol. For EBSD, the sample was mounted on 45 degrees using a pre-tilted polarizer and totally tilted to 70 degrees. An acceleration voltage of 20 kV was set for the EBSD analysis, and the vacuum pressure was maintained below $1 \cdot 10^{-5}$ Torr. EBSD analysis with a step size of 0.5 μm was conducted in the 50 × 80 μm^2 analyzed area. EDS and EBSD maps were processed and rendered using Oxford AZtec and AZtecCrystal (Aztec, Oxford Instruments, High Wycombe, UK) analysis software packages.

Scanning transmission electron microscopy (STEM).—A TEM lamella was prepared via focused ion beam (FIB) milling taken from the exposed sample cross-section (Thermo Fisher Scientific Scios 2 DualBeam FIB-SEM). Prior to FIB, a protective Pt layer was first deposited on the surface using the electron beam (lower energy), and then another Pt layer was deposited using the ion beam prior to FIB milling. These protective Pt layers minimize damage to the surface of the sample by the incident Ga^+ ions. Ion beams of 30 kV per 3 nA and 30 kV per 0.3 nA were then used for cutting the surface and early-stage milling, with a probe size of 81 and 33 nm, respectively. An ion beam of 5 kV per 14 pA was used for the final cleaning step. Additionally, the cross-section was inspected for depth of pores and composition via secondary electron imaging(SEI) at 5 kV and 0.1 nA.

Scanning transmission electron microscopy (STEM) investigation was conducted on a Thermofisher Scientific ThemIS image-corrected microscope at 300 kV equipped with a Bruker SuperX energy dispersive X-ray spectroscopy (EDS) detector. The Bruker windowless detector allows for high count rates with minimal dead time and fast STEM-EDS mapping. The high-speed Ceta2 camera can acquire 4k × 4k images at 40 frames per second for in situ movies. Velox software was used to acquire and process STEM-EDS spectrum image data on the Themis TEM. The quantification process in Velox™ applies "Brown-Powell" ionization cross-section parameterization to obtain the k-factor [1,2] using all the default factors and parameters provided by the manufacturers (Thermofisher Scientific) in the Velox™ software to compare the quantitative results.

X-ray diffraction.—The chemical and phase composition of the residual salt was examined using the Malvern-Panalytical Empyrean diffractometer [wavelength Cu Kα (1.5405 Å)]. The PDF4+ database was employed as the reference data. For Rietveld refinement, the software HighScore Plus was utilized where the pseudo-Voigt function was used to refine the peak profile. It is important to recognize that XRD data from residual salts may not accurately reflect the molecular structure of species in their molten state, given that cooling could induce phase transitions upon solidification. However, analyzing these data enables the detection of the presence of Ni and Cr species in the molten salt, which is one primary focus of this work.

Inductively coupled plasma-mass spectrometry (ICP-MS).—To quantify Cr and Ni contents in FLiNaK salts using the ICP-MS method, approximately 0.22 g of the FLiNaK samples were dissolved into 100 ml of deionized (DI) water. This solution was subsequently analyzed using the mass spectrometer. To ensure accuracy and calibration, standard solutions of Ni (MSNI-100PPM-125 ml, Inorganic Ventures) and Cr (MSCR(3) −100PPM-125 ml, Inorganic Ventures) consisting of 2vol.% of nitric acid were used as baselines. Multiple standard solutions were then fabricated by dilution in DI water and subsequently sonicated for 15 min to achieve homogeneity. Concentrations for these standards were set at 100, 50, 25, 10, and 1 ppb for both Ni and Cr. DI water was employed as a blank so that any background readings emanating from the instrument can be subtracted. The result is shown in Table S1. Additionally, the ICP-MS result of the as-prepared FLiNaK salts was also consistent with the Ni and Cr composition specified in the certificate of analysis provided by the commercial supplier shown in Table S2, showing approximately 0.67 ppm of Cr and 2.42 ppm of Ni.

Results

Thermodynamics and kinetics for Ni20Cr dissolution.—The possibility of bicontinuous dealloying in Ni20Cr alloys within molten FLiNaK was initially explored through the identification of electrochemical potential ranges where only Cr is dissolved as Cr(II) or Cr(III) and Ni remains stable in its zero-valence state. To guide choice of the relevant potential ranges, a one-dimensional phase stability diagram for Ni20Cr was calculated at 600 °C for Ni, Ni(II), Cr, Cr(II), and Cr(III) in FLiNaK relative to the K^+/K potential, presented in Fig. 1a.[6,9] It is noted that all thermodynamic calculation are first calculated relative to the E_{redox} of F_2/F^- assuming a zero E^o_{redox} at 600 °C, then the E_{redox} of all half-cell redox reactions are calculated also considering the activity of Cr and Ni in Ni20Cr(wt%) alloy at 600 °C in terms of $V_{F2/F-}$, which is then calibrated with the

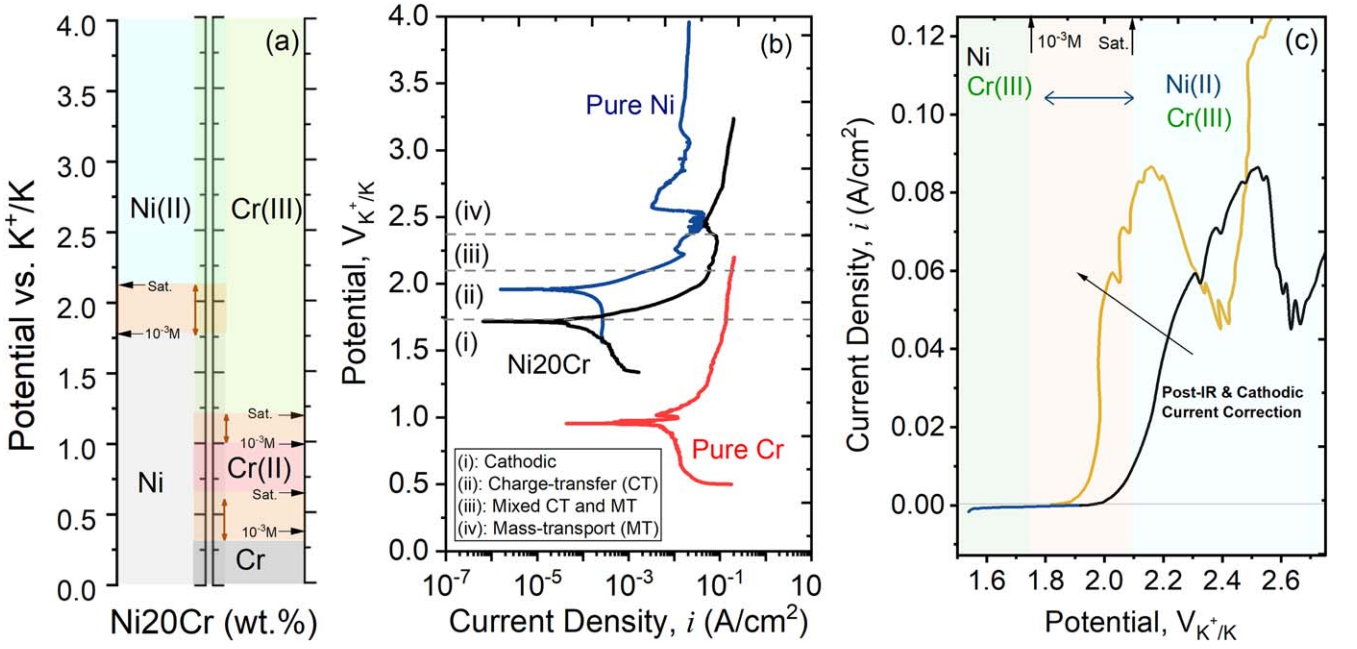

Figure 1. (a) The one-dimensional phase stability diagram for Cr, Ni, Cr(II), Cr(III), and Ni(II) species calculated assuming a F^- ion activity (a_{F-}) of 49.3 M at 600 °C and using the activity of Cr and Ni in Ni20Cr (wt%). Horizontal black arrows on the diagram represent phase boundaries based on an assumed species concentration, while the double-headed vertical arrow highlights the range of phase boundary conditions, extending from 10^{-3} M to bulk saturation. (b) and (c) display the experimental polarization curves for pure Ni, Cr, and the Ni20Cr alloy in the form of linear sweep voltammograms at 1 mV s^{-1}. (c) illustrate the polarization curve for the Ni20Cr alloy, both in its as-measured state and after corrections for iR and cathodic current density.

calculated E_{redox} of K^+/K reaction of -4.63 $V_{F2/F-}$.[9] The E_{redox} of Cr/Cr(II), which Cr(II) and Cr(III) are considered as CrF_3^- or CrF_6^{3-},[6] is found to be highly favorable above +0.27 $V_{K+/K}$. The E_{redox} of Cr(II)/Cr(III) becomes is favorable above +0.67 $V_{K+/K}$.[6,46] In scenarios where Ni(II) is absent or an impurity (assumed to be 10^{-3} M), the E_{redox} of Ni/Ni(II) is calculated to be +1.75 $V_{K+/K}$. The calculated E_{redox} of Ni/Ni(II) redox reaction was verified experimentally via a series of diagnostic CV on a Pt wire electrode with incremental addition of NiF_2 from 0.05 to 1 wt% in FLiNaK salts. The results, as shown in Fig. S3, reveal a bulk saturation limit of approximately ~0.1 wt% NiF_2 with an E_{redox} of ~2.1 $V_{K+/K}$, which is also marked in Fig. 1a. For a more in-depth elaboration on the kinetic properties of NiF_2 or Ni(II) in FLiNaK, readers are referred to a recent study by Smith et al.[47] These thermodynamic redox potentials can guide understanding of E-log(i) corrosion behavior.

Figure 1b depicts the E-log(i) curve of Ni, Ni20Cr, and Cr in molten FLiNaK at 600 °C. The LSV of Cr in molten FLiNaK was investigated previously.[25] High purity Ni displays a very similar qualitative E-log(i) behavior when compared to Cr except shifted to more positive potentials, characterized by the presence of both charge-transfer (CT) and mass-transport (MT) E-log(i) regimes,[13,48] The latter may be attributed to the formation of K-Ni-F salt film due to the low solubility of NiF_2 (<0.1 wt%).[49] The E_{oc} values for Ni and Cr differ by approximately 1.3 V due to their significant difference in thermodynamic stability.[2,9] The anodic polarization regime of Ni20Cr (wt%) is CT-controlled over a ~300 mV range between +1.72 $V_{K+/K}$ and +2.05 $V_{K+/K}$, followed by a mixed CT and MT-controlled regime to +2.32 $V_{K+/K}$, and eventually reaches a limiting current density. Each kinetic regime pertaining to the electrodissolution step is separated by a dashed horizontal line and labeled accordingly: (i) cathodic, (ii) CT, (iii) mixed CT and MT, and (iv) MT. It is noted that the potential domain for cathodic regimes is dependent upon factors, including the oxidizers present, temperature, and convection effects.[25,50] Figure 1c shows the i-E curve of Ni20Cr before (dark) and after (yellow) iR and cathodic current density correction, overlaid with color maps to indicate potential ranges where Cr(III) and Ni(II) are stable. As predicted in Fig. 1a, the potential up to +1.75 $V_{K+/K}$ is the region in which only Cr dissolves. The boundary gradually increases up to +2.134 $V_{K+/K}$ as Ni begins to dissolve, saturating in FLiNaK and shifting E_{redox}. Above +2.134 $V_{K+/K,}$ it is predicted that both Cr and Ni dissolve.

Figure 1 indicates that dealloying can occur solely through Cr dissolution, and also at a more positive potential with Cr exhibiting high rates and Ni showing lower rates, differing by three orders of magnitude. The implications align with classical interpretations derived from aqueous studies. Specifically, the greater the difference in equilibrium oxidation reactions between Cr and Ni, the easier it is to dealloy, especially when there is thermodynamic immunity of Ni. In this scenario, the ratio of dealloying front velocity to uniform corrosion front velocity approaches infinity.

Morphological evolution with applied potential.—Ni20Cr (wt%) alloys are potentiostatically held in FLiNaK at 600 °C over a 1 V potential range at +1.75, +1.90, +2.10, +2.30, +2.50, and +2.75 $V_{K+/K}$ for 10 ks. The post-corrosion surface morphologies in plan view are examined using SEM as shown in Fig. 2. In Figs. 2a–2c, which correspond to Ni20Cr alloys polarized at +1.75, +1.90, and +2.10 $V_{K+/K}$, respectively, the plan view surface exhibits microporosity coupled with interconnected discrete ligaments. This potential regime falls within the CT-controlled in which the oxidation step produces rapid dissolution where $i_{anodic} \sim \exp(E_{app})$ and Ni remains thermodynamically stable (Fig. 1a), or dissolves at a significantly slower rate relative to Cr (Fig. 1b). The presence of an interconnected pores-ligaments network indicates that bicontinuous dealloying can occur in the Ni20Cr alloy in FLiNaK at 600 °C. One point of note is that the ligament features are similar to the case of molten chloride dealloying[15–20,32,33] and liquid metal dealloying,[51] but are significantly coarser relative to the features observed upon dealloying of Cu-Zn, Ag-Au, and Pt-Ni alloys in aqueous solution such as $HClO_4$,[22] H_2NO_3,[52] and others,[53,54] surmised to be due to the

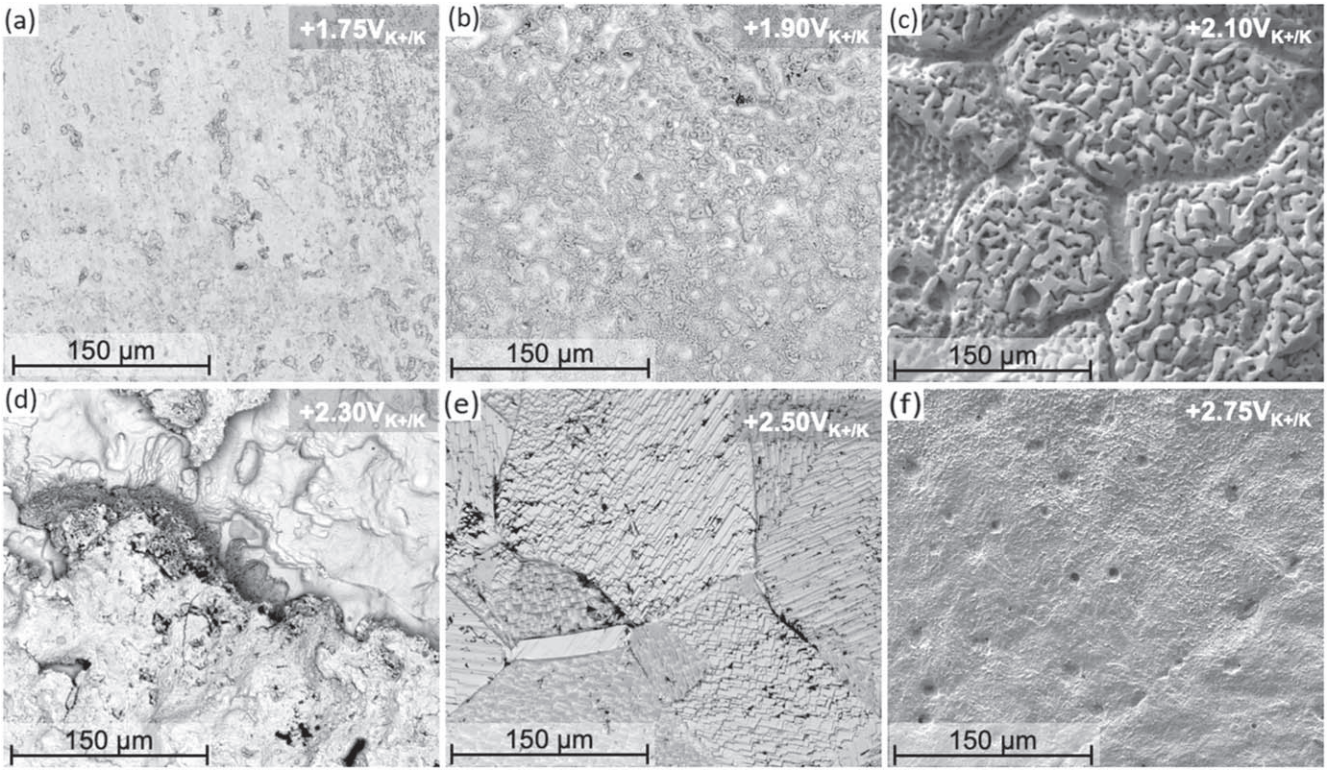

Figure 2. Representative backscattered electron micrographs depicting the plan-view surfaces of Ni20Cr (wt%) subjected to potentiostatic polarization conditions: (a) at +1.75 $V_{K+/K}$, (b) at +1.90 $V_{K+/K}$, (c) at +2.1 $V_{K+/K}$, (d) at +2.3 $V_{K+/K}$, (e) at +2.5 $V_{K+/K}$, and (f) at +2.7 $V_{K+/K}$. The alloys were exposed to molten FLiNaK salts at a temperature of 600 °C for a duration of 10 ks.

high homologous temperature in the case of molten salts. Given that the potentials of +1.75, +1.90, and +2.10 $V_{K/K+}$ indicate bicontinuous dealloying, additional electrochemical and morphological characterization was performed, as presented in Fig. 3–8.

As the applied potential increases, a gradual diminishment of the microporous morphology is observed, transitioning into different corrosion morphologies as evidenced in Figs. 2d through 2f. When polarized at +2.30 $V_{K+/K}$ and +2.50 $V_{K+/K}$ for 10 ks, Ni20Cr alloys are found to exhibit grain surfaces that are relatively sharp, rough and appeared crystallographically jagged. Some interconnected ligaments are observed in the +2.30 $V_{K+/K}$ sample, as shown in Fig. S4. Conversely, no porous structure is detected in the +2.50 $V_{K+/K}$ sample; instead, grains with sharply visualized facets were seen. These facets are interpreted as manifestations of direct and rapid dissolution of both Cr forming Cr(III) and Ni(II), revealing facets formed by different crystallographic orientations.[25] Between +2.30 $V_{K+/K}$ and +2.50 $V_{K+/K}$, both Ni and Cr dissolve governed by a mixed CT- and MT- controlled dissolution. Lastly, at 2.75 $V_{K+/K}$, the dissolution of Ni20Cr is controlled by MT at the limiting current density (i.e. maximum dissolution rate), yielding a relatively smooth surface containing surface-level micropores.[25,55] The smooth surface implies that the Ni20Cr substrate could be dissolving underneath a salt film, formed in situ by the saturation of Cr(III)-F and Ni(II)-F compounds on the surface, whereby the microstructural effect on alloy dissolution is believed to be negligible at the MT limit. It is noted that grain boundary (GB) dissolution is observed at the potentiostatic polarization potentials between +1.90 $V_{K+/K}$ and +2.50 $V_{K+/K}$; A follow-on work will be conducted to investigate the behavior of grain boundary dissolution during potentiostatic dealloying.

In-operando electrochemical and microstructural characterizations.— *Dealloying at +1.75$V_{K+/K}$.*—At +1.75 $V_{K+/K}$ (Fig. 3a), only Cr is expected to dissolve, forming Cr(III), while Ni dissolution is not thermodynamically favorable. In Fig. 3a, a constant anodic $i_{electric}$ is observed and sustained at $\sim10^{-5}$ A cm^{-2} until reaching ~4 ks, at which point the $i_{electric}$ decreases and fluctuates between 10^{-6} A cm^{-2} and 10^{-8} A cm^{-2}. Up until this point, 0.33 μm of Cr may have dissolved according to Eq. 5 assuming 0% remaining Cr in ligaments neglecting porosity. Due to the close proximity of E_{oc} (~1.7 $V_{K+/K}$) to this applied potential, the drop in $i_{e.}$ is likely associated with the cathodic reduction of Cr(III)/Cr(II) becoming kinetically dominant (i.e. more Cr(III) available to be electrochemically reduced), resulting in a decrease in net i.e..[13,25,41,56,57] This behavior is further validated in Fig. S5.

Confirmation of this thermodynamic prediction is provided by *in situ* CV measurements on the secondary Pt WE, as shown in Fig. 3b. Redox reactions associated with Cr/Cr(II) and Cr(II)/Cr(III) are possible in the potential range of +0.1 to +1.2 $V_{K+/K}$ (shaded red region), while reactions for Ni/Ni(II) in the potential window from +1.50 to +2.25 $V_{K+/K}$ (shaded blue region) are absent. For clarity, only the CV scan conducted before and after 10ks of pstat dealloying is shown in Fig. 3b to identify the presence of Cr and/or Ni species in salt. All CV plots between 1ks and 10ks at 1.75, 1.90, and 2.10 $V_{K+/K}$ are shown in Fig. S6.1.

Regarding Fig. 3c, the impedance spectra of the test sample can be fitted with an EEC, containing R_s as the solution resistance, R_1 as the charge-transfer resistance (R_{ct}), and the constant phase element CPE_1 as the double-layer capacitance (C_{dl}). As the duration of potentiostatic hold progressed, an increase in the semicircles on the Nyquist plot was observed, indicating a rise in R_{ct} as detailed in Table S3. This change in impedance behavior points to the surface becoming more electrochemically resistive, potentially as a result of the depletion or encapsulation of Cr within the Ni ligaments spreading by surface diffusion.[19] This phenomenon is marked by Ni exhibiting low dissolution rates and/or remaining stable at these potentials. It is noted that, for simplicity, only impedance results for intervals from 2 ks to 10 ks (in increments of 2 ks) are shown here. However, all of these data, along with the fitted Bode plots, can be accessed in Fig. S6.2 and Tables S4 through S5.

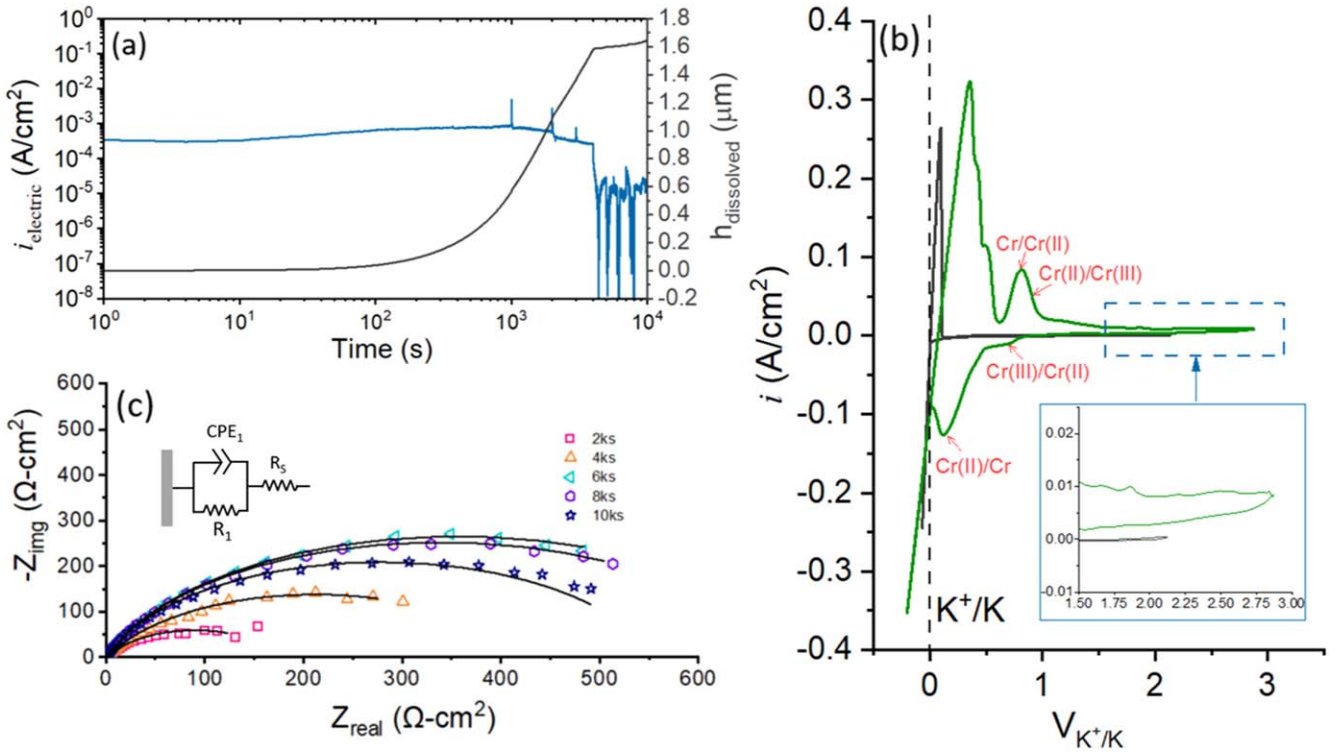

Figure 3. Ni20Cr (wt%) subjected to potentiostatic hold in molten FLiNaK at 600 °C at +1.75 $V_{K+/K}$. (a) display the current time relationship, (b) shows the cyclic voltammogram measured the secondary Pt WE before (black) and after 10 ks of potentiostatic hold of Ni20Cr. The redox peaks of possible Cr/Cr(II) and Cr(II)/Cr(III) reactions are labeled. The inset in (b) highlights the potential range in which the Ni/Ni(II) half-cell redox reactions are possible (c) shows the Nyquist plots measured at each 2 ks time increment containing the EEC used for fitting analysis and fitting results (black lines).

Figure 4a shows that the Ni20Cr (wt%) surface, potentiostatically polarized at +1.75 $V_{K+/K}$ for 10 ks, revealing two distinct grains. One grain exhibits a dealloyed bicontinuous porous structure, while the other appears to be partially dealloyed. The dealloyed grain exhibits an interconnected network of nano-pores and sub-micron-sized ligaments, with a measured width of 0.29 ± 0.08 μm. Three distinct locations were analyzed with EDS point analysis as shown in Fig. 4b and Table I. Point #1, located on a ligament, contained 3.7 wt % Cr above a Ni-rich substrate (Point #2) with 16.2 wt% Cr, while the partially dealloyed grain at Point #3 possessed 7.5 wt% Cr. It is noted that the EDS point analysis serves to qualitatively correlate select surface features and approximate composition. Due to the size of the interaction volume relative to the submicron dealloying features, the results in Table I are averaged and estimated values.

The cross-section of the ligament is further examined in Figs. 4c and 4f. The sample exhibits a top dealloyed layer with a measured depth of 0.81 ± 0.18 μm, which is higher than the calculated $h_{dissolved}$ presented in Fig. 3a. The discrepancy, where $h_{dissolved}$ is underestimated, can be attributed to the net $i_{electric}$ at this potential being close to zero due to the progressive dominance of cathodic current densities. This top layer reveals nanoporosity that is Ni-enriched (Fig. 4d). Notably, the interface between this top layer and the bulk Ni20Cr substrate was characterized by interconnected micro-voids, suggesting poor adhesion of the Ni enrichment layer to the underlying substrate.[15,58,59] Line scan data delineate the concentration profiles of Ni and Cr at the near-surface region, revealing the depletion of Cr with a residual presence of about 5 wt % within the layer and a concentration profile that is 0.57 μm wide. A critical observation from this study is that the bicontinuous morphological evolution is restricted to the top layer, with no significant penetration into the deeper alloy substrate at this dealloying potential and time. The role of grain boundaries is to be addressed elsewhere.

Figure 4g shows the inverse pole figure (IPF) map from a different cross-sectional area of the sample. Two adjacent grains both nearly aligned with the $(001)_{FCC}$ are shown in Fig. 4g. Sub-micron sized segments that take on various crystal orientations are displayed within the top enrichment layer. It is noted that Ni deposition (i.e. the reduction reaction from Ni(II) to Ni) is not thermodynamically favorable at this potential. Therefore, the shift of crystallographic orientation of grain cross-section near the top surface may be triggered by the combination of surface rearrangement and grain boundary reorientation for the minimization of internal energy once Cr is depleted; a similar behavior was observed by Ghaznavi, Persaud, and Newman.[15,19,20]

Dealloying at +1.90 $V_{K+/K}$.—At +1.90 $V_{K+/K}$ (Fig. 5d), the anodic $i_{electric}$ remains relatively constant at $\sim 10^{-2}$ A cm^{-2} throughout the 10 ks polarization duration, estimating an $h_{dissolved}$ of 11 μm based on Eq. 5.

At this potential, both Ni and Cr are thermodynamically favorable to dissolve, though Ni dissolves at least three orders of magnitude slower than Cr, as evidenced in Fig. 1b at the potential of +1.90 $V_{K+/K}$. Figure 5b illustrates the occurrence of Cr/Cr(II)/Cr(III) redox reactions within the potential window of +0.1 V to +1.0 $V_{K+/K}$, and Ni/Ni(II) redox reactions in the range of +1.50 to +3.00 $V_{K+/K}$.[47,56] It is noted that possible oxidation peaks are visible observed in vicinity to the Ni/Ni(II) peaks. This may be attributed to the polycrystalline nature of the Pt wire and the possible formation of Ni-Cr-F complex species, which has yet to be investigated in this salt environment.

The Nyquist impedance spectra (Fig. 5f) can also be fitted with an EEC comprising of R_s connected in series with two-time constants (CPE_1/R_1 & CPE_2/R_2). The first time constant (CPE_1/R_1) is used to describes the slightly depressed semicircle at the high frequency region, possibly attributed to the dispersion or

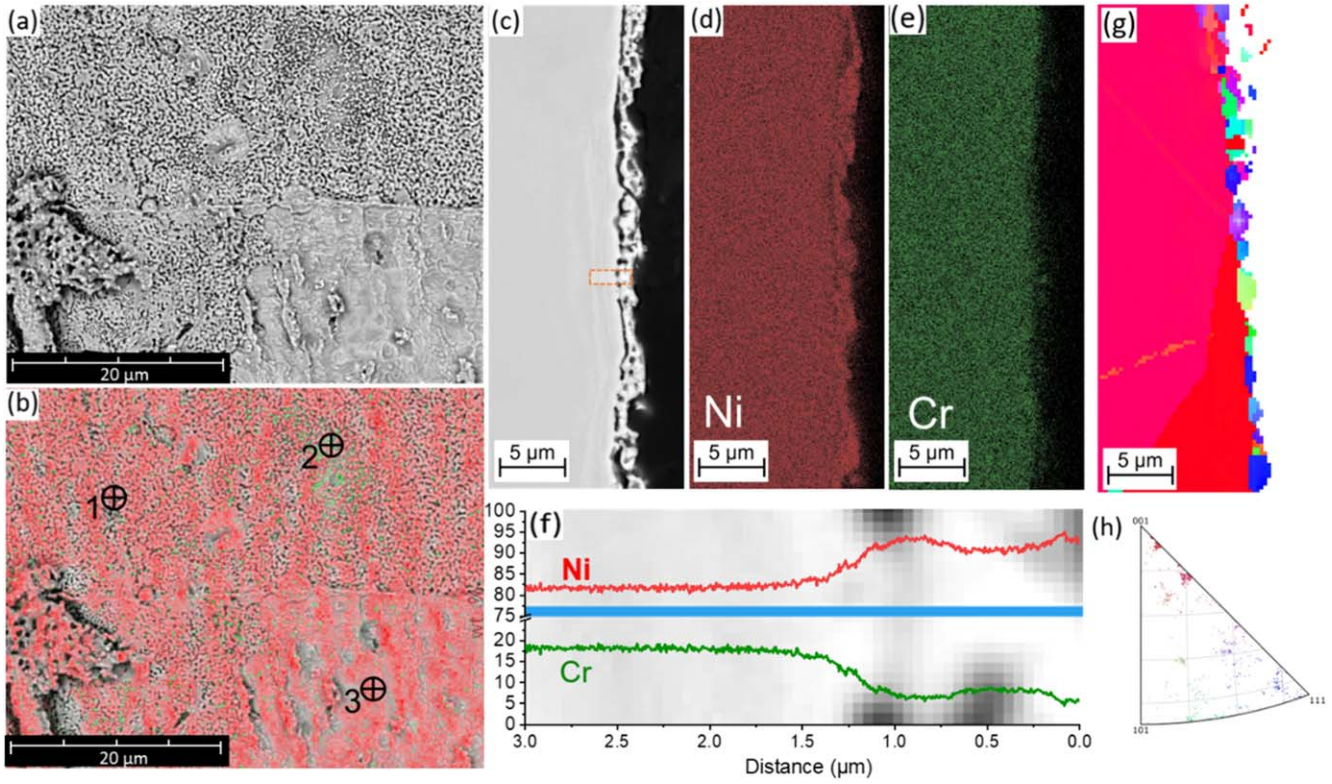

Figure 4. Ni20Cr (wt.%) potentiostatically polarized at +1.75 $V_{K+/K}$ for 10 ks. (a) Plan-view SEM image showing surface morphology. (b) Composite EDS elemental maps overlaid on SEM image, highlighting Ni (red) and Cr (green) distribution. Specific locations were marked for point analysis. (c) Cross-sectional SEM image of the sample. (d) and (e) EDS maps for Ni (red) and Cr (green), respectively. The semi-transparent rectangle in (c) indicates the area subjected to EDS line scan analysis, with corresponding elemental profiles for Ni and Cr presented in (f). EBSD analysis is shown via the inverse pole figure (IPF) plot of a separate cross-sectional surface in (g). The stereographic triangle in (h) marks the orientation of the grains present in (g).

Table I. Plan-view EDS point analysis on Ni20Cr (wt.%) upon potentiostatic hold at +1.75 $V_{K+/K}$, +1.90 $V_{K+/K}$, and +2.10$V_{K+/K}$ for 10 ks in molten FLiNaK, 600 °C.

Point #	1.75 $V_{K+/K}$		1.90 $V_{K+/K}$		2.10 $V_{K+/K}$	
	Ni (wt %)	Cr (wt %)	Ni (wt %)	Cr (wt %)	Ni (wt %)	Cr (wt %)
1	96.3	3.7	100	0	98.0	2.0
2	83.8	16.2	88.1	11.9	79.8	20.2
3	92.5	7.5	97.7	2.3	84.6	15.4

nanoporosity, whereas the second time constant (CPE_2/R_2) described the low frequency semicircle that exhibits a very similar impedance magnitude as seen at +1.75 V. The origin of the second time constant is still being investigated, but another possible origin is the formation of localized salt film in FLiNaK.[7,16,25] Due to this uncertainty, the R_{ct} was estimated by the summation of R_1 and R_2.

As illustrated in Fig. 6a, the post-dealloying surface of Ni20Cr at +1.90 $V_{K+/K}$ for 10 ks presents a coarser interconnected ligament structure with a width of 0.95 ± 0.15 μm. Beneath these coarser features, finer submicron ligaments are visible. According to the EDS point analysis detailed in Table I, the ligament consists entirely of pure Ni (Point #1), an undealloyed bare surface with 11.9 wt% Cr (Point #2), and the grain boundary, which contains 2.3 wt% Cr (Point #3). It is important to note that, in contrast to Fig. 4a, the ligaments appear somewhat directional, indicating a possible influence of crystallographic orientation, which will be discussed later.[19,21]

The cross-sectional characterizations from Figs. 6c–6e unveils a distinct top layer enriched with Ni and infiltrated with residual fluoride salts. This layer, with a measured thickness of 10.9 ± 3.45 μm, displays notable micro-porosities and curvature, which may correlate with the coarser ligament structure identified, and a non-uniform interface between the top Ni layer and the substrate. Additionally, the cross-section thickness also closely matches the $h_{dissolved}$ calculated in Fig. 5b. Figure 6c also captures a grain boundary that exhibits some level of dissolution. Grain boundary dissolution was deeper at this potential, however it does not seem to significantly influence the intragranular dealloying process located ~100 μm laterally away from grain boundaries. Furthermore, EDS line scan analysis reveal a complete depletion of Cr in the ligaments, with a concentration profile extending 1 μm in width.

Figure 6h shows the IPF from another cross-section location that contains two adjacent grains with orientations close to $(103)_{FCC}$ and within 5 degrees of $(101)_{FCC}$. Localized segments sized between 0.5 and 2 μm at the alloy surface display different crystallographic orientations than their parent grains. For instance, on the $(103)_{FCC}$ grain, small regions with directions closer to $(110)_{FCC}$ and $(111)_{FCC}$ are seen. A similar argument can be made regard to the minimization of internal and surface energy via Ni coarsening (due to surface diffusion) and CSL grain boundary formation.[15] Although the possibility of Ni plating onto Ni20Cr at 1.9 $V_{K+/K}$ in FLiNaK was initially considered, subsequent findings (Fig. S7) refute this assumption therefore attributing the surface near orientation to grain restructuring rather than surface plating.

On the effect of time, Fig. 7 displays the plan view morphological a Ni20Cr sample sequentially potentiostatically held at +1.90 $V_{K+/K}$ for 1, 3, 5, and 10 ks in FLiNaK at 600 °C, utilizing the same sample to guarantee consistency in observing time-dependent changes. The initial state at 1 ks (Fig. 7a) shows minimal corrosion, yet a closer inspection at 10,000x magnification (Fig. 7b) reveals the formation of granulated surface texture, signaling initial material dissolution with an estimated depth of 1.18 μm as determined from Fig. 5a. After 3 ks, both grains and grain boundaries become visually distinguishable (Fig. 9c), suggesting some etching effect, although the sample preparation scratches remain. Figure 9d, at 10,000x magnification, shows surface features resembling those observed at

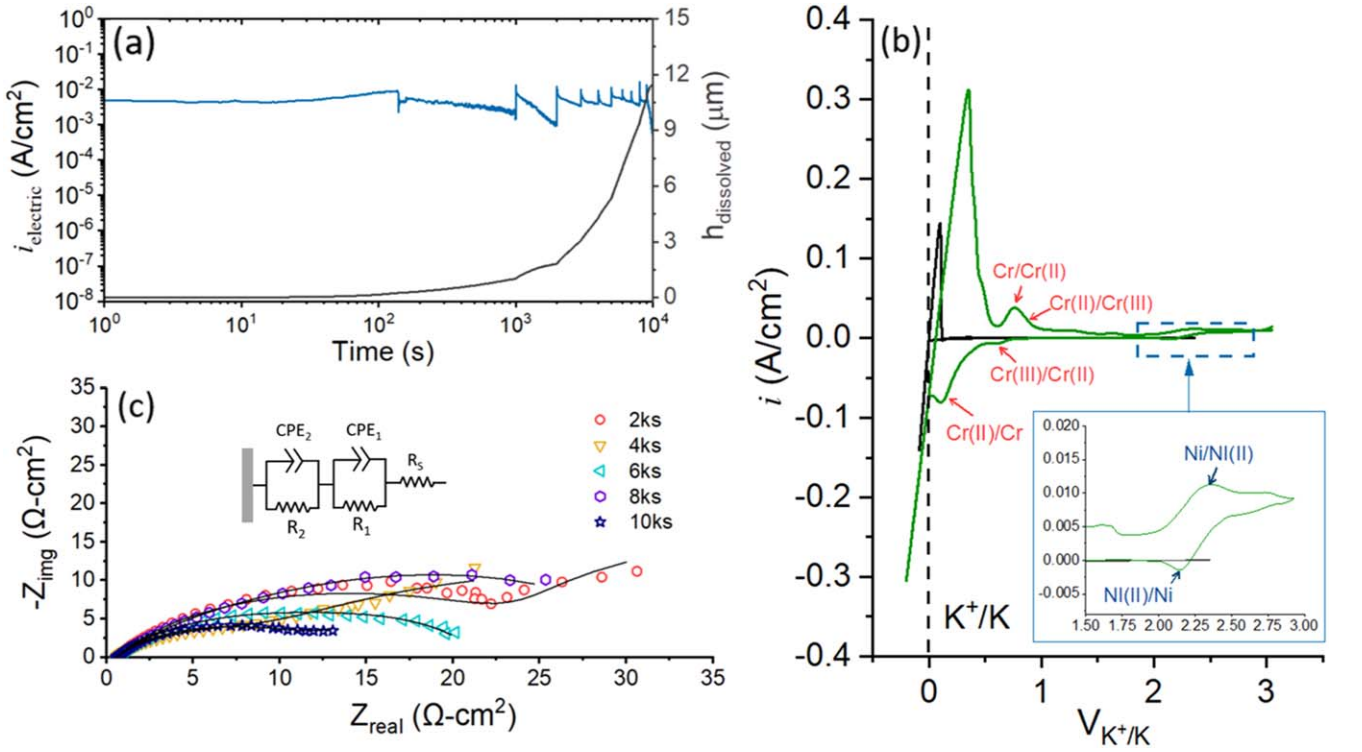

Figure 5. Ni20Cr (wt%) subjected to potentiostatic hold in molten FLiNaK at 600 °C at +1.90$V_{K+/K}$. (a) display the current time relationship, (b) shows the cyclic voltammogram measured the secondary Pt WE before (black) and after 10 ks of potentiostatic hold of Ni20Cr. The redox peaks of possible Cr/Cr(II), Cr (II)/Cr(III), Ni/Ni(II) reactions are labeled. The inset in (b) highlights the potential range in which the Ni/Ni(II) half-cell redox reactions are possible (c) shows the Nyquist plots measured at each 2 ks time increment containing the EEC used for fitting analysis and fitting results (black lines).

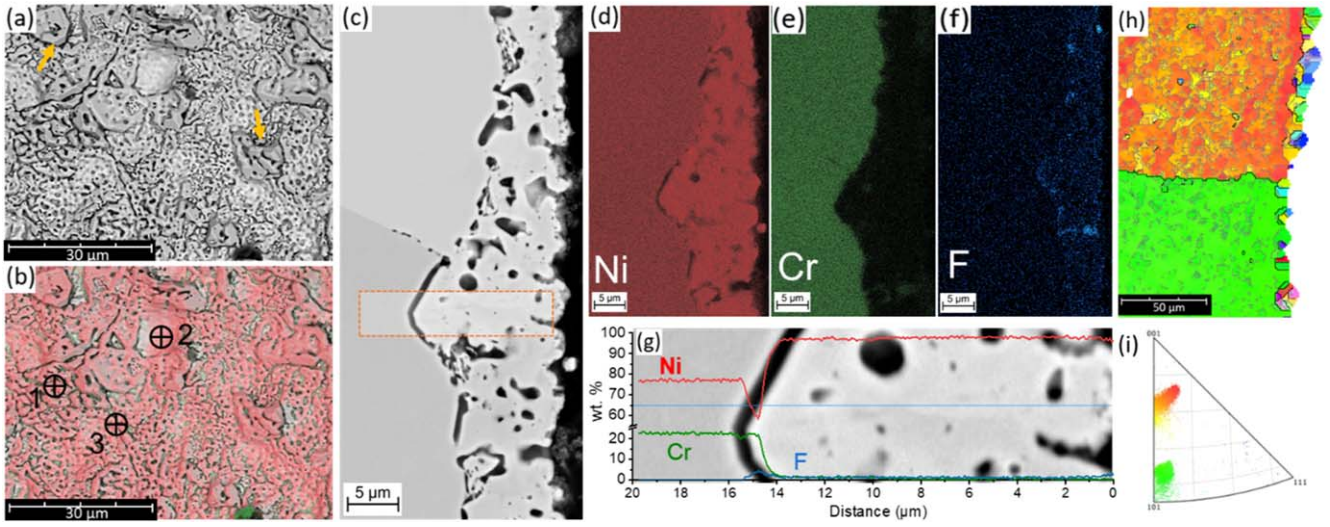

Figure 6. Ni20Cr (wt.%) potentiostatically polarized at +1.90 $V_{K+/K}$ for 10 ks. (a) Plan-view SEM image showing surface morphology. (b) Composite EDS elemental maps overlaid on (a), highlighting Ni (red) and Cr (green) distribution. Specific locations were marked for point analysis. (c) Cross-sectional SEM image of the sample. (d), (e), (f) are EDS maps for Ni (red), Cr (green), and F (blue) respectively. The semi-transparent rectangle in (c) indicates the area subjected to EDS line scan analysis, with corresponding elemental profiles for Ni and Cr presented in (g). EBSD analysis is shown via the inverse pole figure (IPF) plot of a separate cross-sectional surface in (h). The stereographic triangle in (i) marks the orientation of the grains present in (h).

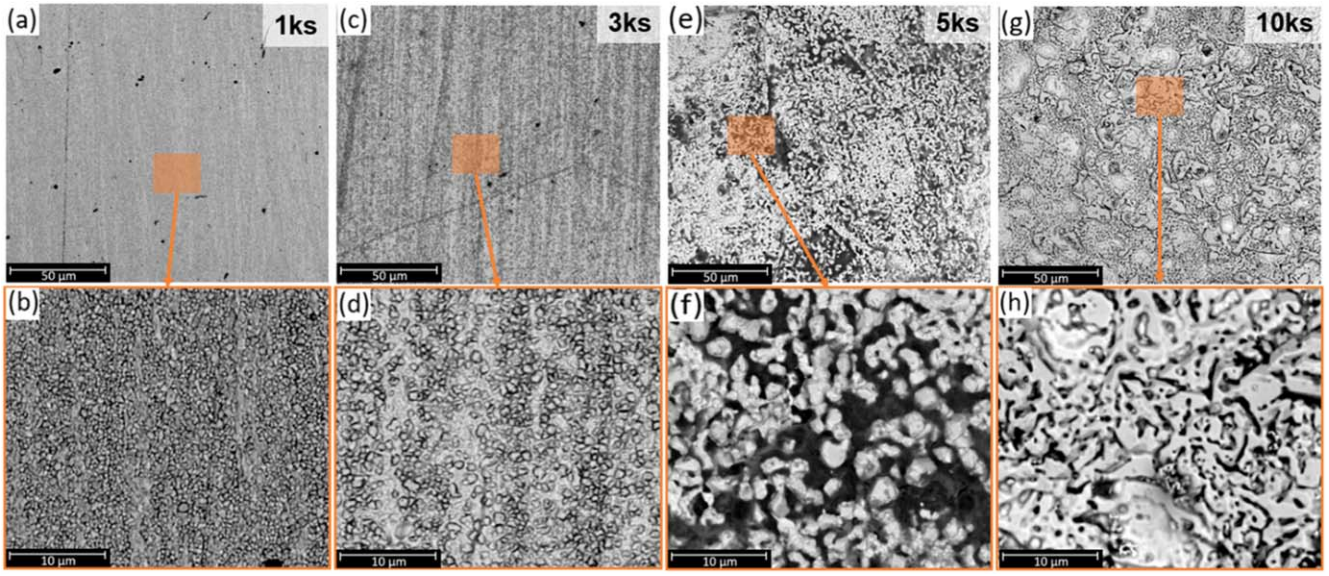

Figure 7. Backscattered electron micrographs of Ni20Cr potentiostatically held at +1.90$V_{K+/K}$ for (a) 1 ks, (b) 3 ks, (c) 5 ks, and (d) 10 ks in molten FLiNaK salts, 600 °C taken at 2,000x magnification. (e), (f), (g), and (h) display the 10,000x magnified region of (a), (b), (c), and (d), respectively.

1 ks but with a coarser appearance. By 5 ks, bicontinuous dealloying morphologies emerge, with up to 5.36 μm of total dissolved materials, and the grain surfaces exhibit either micro-scale rectangular pits—similar to features noted in pure Cr samples affected by salt attacks–or micro-porosities (Fig. 7f), with darker spots among the ligaments indicating residual salt presence. Lastly, after 10 ks of ligament coarsening,the ligament features became distinct.

Dealloying at +2.10 $V_{K+/K}$.—At +2.10 $V_{K+/K}$ (Fig. 8a), both Ni and Cr rapidly dissolve at a significant rate, resulting in a $h_{dissolved}$ of 44.5 μm. Both Ni and Cr corrosion products were detected by the in situ CV measurements as shown in Fig. 8b, consistent with thermodynamic predictions. The $i_{electric}$ starts near 10^{-1} A cm^{-2}, gradually reduces an order of magnitude to 10^{-2} A cm^{-2} starting at 1 ks, but remains overall anodic. In Fig. 8c, the Nyquist impedance spectra behave as a highly depressed semicircle, in both low and high frequency domains, dominated by the CT process due to the accelerated dissolution of both Ni and Cr. It is worth noting that the Nyquist plot gradually shifts upward (i.e. larger imaginary and real impedance) as time elapsed. The impedance spectra can be fitted with the EEC used for the +1.90 $V_{K+/K}$ sample with possibly identical attributes for the first time constant. However, the second time constant is found to exhibit an α value of 0.45 (see Table S4), suggesting that the low frequency domain (or depressed semicircle) may be attributed to the diffusional impedance mediated by the salt film[60,61] which imposes mass-transport controlled behavior the authors previously observed.[25,57] This phenomenon is further investigated and interrogated via with STEM analysis shown in Fig. S8.

Figures 9a and 9b display bicontinuous dealloying features similar to Fig. 6 where the polarization was at +1.90 $V_{K+/K}$. The coarsening and faceting of surface Ni ligaments are more

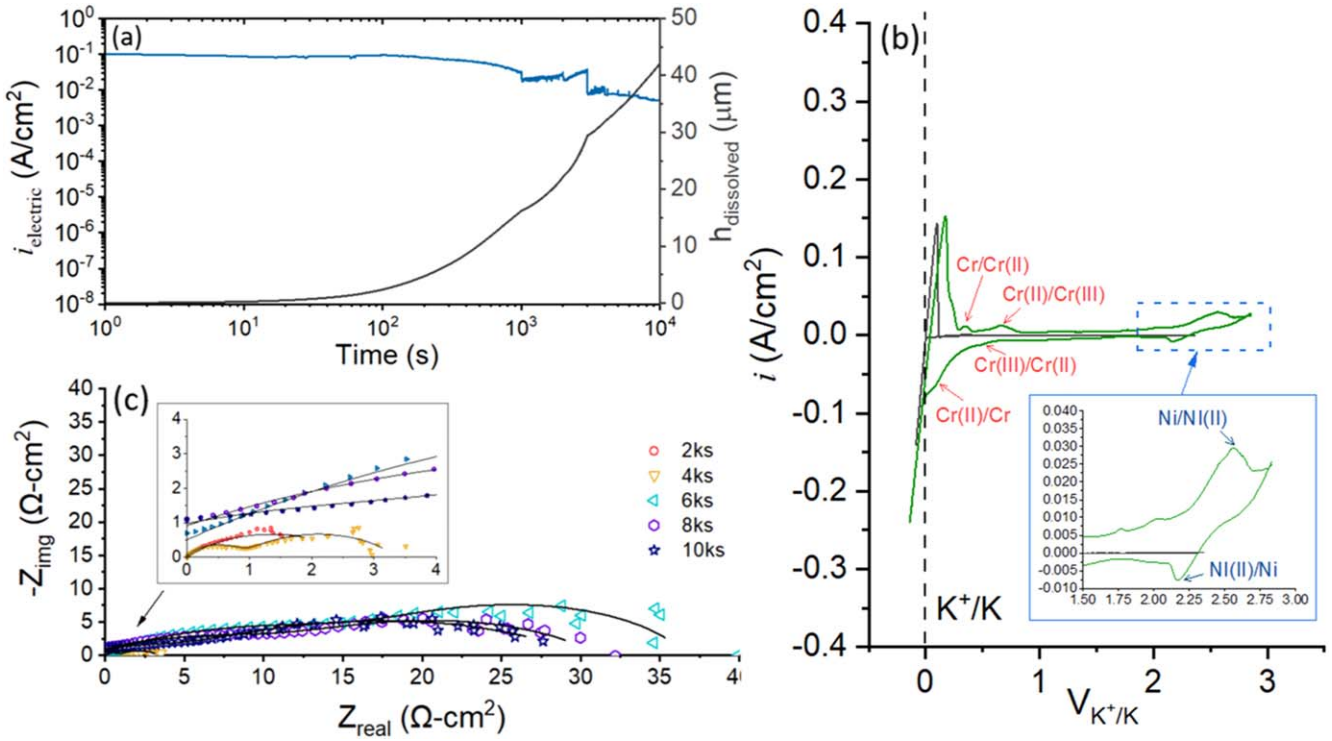

Figure 8. Ni20Cr (wt%) subjected to potentiostatic hold in molten FLiNaK at 600 °C at +2.10 $V_{K+/K}$. (a) display the current time relationship, (b) shows the cyclic voltammogram measured the secondary Pt WE before (black) and after 10 ks of potentiostatic hold of Ni20Cr. The redox peaks of possible Cr/Cr(II) and Cr(II)/Cr(III) reactions are labeled. The inset in (b) highlights the potential range in which the Ni/Ni(II) half-cell redox reactions areis possible (c) shows the Nyquist plots measured at each 2 ks time increment containing the EEC used for fitting analysis and fitting results (black lines).

pronounced and, to an extent, densified as the micro-porosities become less distinct. The faceted ligaments are 8.99 ± 1.37 μm in width. Grain boundaries show the appearance of trenches comprised of 15.4 wt% of Cr, hinting at preferential dissolution from these regions and possible re-supply by fast-path dissolution. Some ligaments appear detached from the substrate, resulting in the exposure of the bare Ni20Cr (wt%) substrate as verified by the EDS map and the analysis of Point #2 in Fig. 9b.

The cross-sectional analysis in Fig. 9c reveals a significantly coarsened ligament structure on the top surface, which is enriched with Ni (Fig. 9d). The thickness of the dealloyed layer is measured at 12.0 ± 2.83 μm, and the presence of underlying microvoids likely contributed to the poor adherence and detachment of ligaments seen in Fig. 9a. The EDS line scan in Fig. 9g indicated that the top layer is completely depleted of Cr. An EDS line scan was also conducted in a region without salt filtration to obtain the concentration profile of

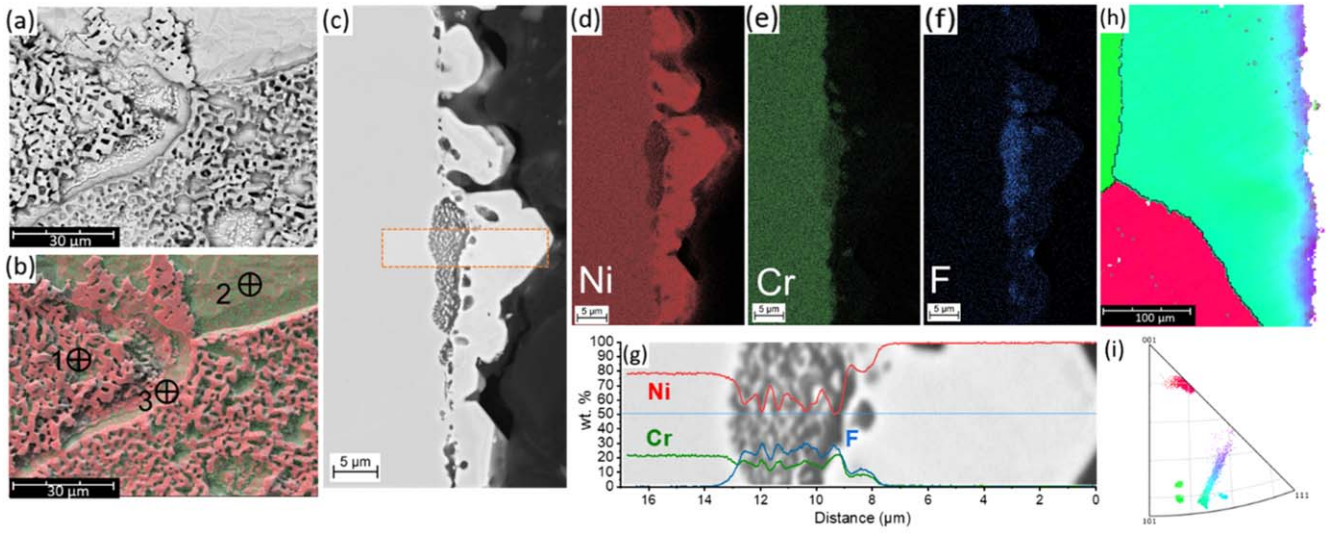

Figure 9. Ni20Cr (wt.%) potentiostatically polarized at +2.10 $V_{K+/K}$ for 10 ks. (a) Plan-view SEM image showing surface morphology. (b) Composite EDS elemental maps overlaid on (a), highlighting Ni (red) and Cr (green) distribution. Specific locations were marked for point analysis. (c) Cross-sectional SEM image of the sample. (d), (e), (f) are EDS maps for Ni (red), Cr (green), and F (blue) respectively. The semi-transparent rectangle in (c) indicates the area subjected to EDS line scan analysis, with corresponding elemental profiles for Ni and Cr presented in (g). EBSD analysis is shown via the inverse pole figure (IPF) of a separate cross-sectional surface in (h). The stereographic triangle in (i) marks the orientation of the grains present in (h).

Cr depletion, with the results further detailed in Fig. S9. Underneath the coarser ligaments, a region about 3 μm in width shows residual fluoride infiltration. In this region, the presence of Ni, Cr, and F suggests the possibility of metal fluoride salt film formation due to salt infiltration and Cr and/or Ni saturation (Fig. S8).[7,49,62]

Lastly, at +2.10 $V_{K+/K}$, the IPF in Fig. 9h reveals two grain orientations close to the —$(001)_{FCC}$ and $(101)_{FCC}$ planes on the top surface. Intriguingly, a transition to the $(111)_{FCC}$ direction is noticeable within the upper 5 μm from the top surface. Given that the original grain size exceeds 100 μm, this change in direction is attributable to the dealloying process rather than the remnants of another grain. The formation and coarsening of the ligaments may also be affected by the crystallographic orientation of the parent grain,[15,19,53] though this relationship is not clearly evident in this work. Nevertheless, it was proven that these features are not a result of possible Ni(II) to Ni plating detailed in Fig. S7.

X-ray diffraction (XRD) of as-solidified salts.—The X-ray diffractogram in Fig. 10 shows that the residual salt after the potentiostatic polarization at +1.75 $V_{K+/K}$ contains oxidized Cr species such as $KCrF_3$, Li_2CrF_6, and K_3CrF_6,[62] though no Ni species are found. This correlates with the results of ICP-MS detection of Cr and Ni (Table S1) and the in situ CV presented in Fig. 3b, where current peaks corresponding to Cr/Cr(II) and Cr(II)/Cr(III) are detected while Ni oxidation and/or reduction peaks are absent. It is noted that the ICP-MS data is collected after the experiment and after the salt is frozen, and therefore it is unclear what the isotope/element concentration was during the liquid salt *in-operando*. With $E_{applied}$ of +1.9 $V_{K+/K}$ and +2.1 $V_{K+/K}$ (Fig. 10), the presence of NiF_2 compounds is detected in the salt together with K_3CrF_6. The obtained results are also in agreement with the CV data for +1.9 $V_{K+/K}$ and +2.1 $V_{K+/K}$ where current peaks for Cr/Cr(II) and Cr(II)/Cr(III) and Ni/Ni(II) were found.

The increase in the $E_{applied}$ to +2.3 $V_{K+/K}$ and +2.5 $V_{K+/K}$ do not influence the salt phase composition (Fig. S10); the salt phase contains Li_2CrF_6, K_3CrF_6, NiF_2, and $NaNiF_3$ compounds, similar to the salt composition after potentiostatic polarization at +1.9 $V_{K+/K}$ and +2.1 $V_{K+/K}$ (Fig. 10). However, when the potential is held at +2.75 $V_{K+/K}$, diffraction peaks corresponding to Ni(III) compounds such as Na_3NiF_6 are also detected (dark blue line in Fig. S10).

Discussion

Dealloying encompasses the outward diffusion of Cr over 10ks from the bulk substrate, across the metal/salt interface to the salt through various transport mechanisms. At room temperature Cr mobility is limited but Cr can more readily diffuse at 600 °C. This process involves a series of sequential and concurrent transport phenomena that elucidate the control mechanisms behind the release of Cr(II) and Cr(III). Transport through the bulk and along grain boundaries facilitates the movement of Cr to areas where Cr is depleted. Furthermore, the interface between the metal and salt, along with the electrochemical double layer, plays a critical role in mediating electrochemical oxidation processes, which are influenced by the CT, MT, or mixed controlled polarization behavior. As the applied potential changes, the rate-determining process that controls the mechanism of Cr transport and subsequent release is altered. While this process is interconnected with the morphology, the $i_{electric}$ and Cr flux alone are inadequate to account for all the controlling factors. The molten fluoride dealloying process supports features characteristic of bicontinuous morphology, notably the formation of an interconnected network of micro-pores and ligaments enriched with the MN element Ni. Interestingly, the ligaments coarsen with increasing applied potential, from 0.29 μm (+1.75 $V_{K+/K}$, 10 ks) and 0.95 μm (+1.90 $V_{K+/K}$, 10 ks) to 8.99 μm (+2.10 $V_{K+/K}$, 10 ks), as shown in Table II. Such potential dependent coarsening has been observed elsewhere[63–66] and will be discussed.

Applied potential effect on surface diffusion.—The dealloying process leaves unoxidized Ni-rich material on the sample surface. However, the remaining material forms ligament features that do not exhibit nanometer porosity but instead coarsen and densify during the dealloying process. To understand whether the coarsening mechanism is solely governed by surface diffusion or concurrently assisted by bulk diffusion, Eq. 7 can be utilized to study the relationship between morphology and time:

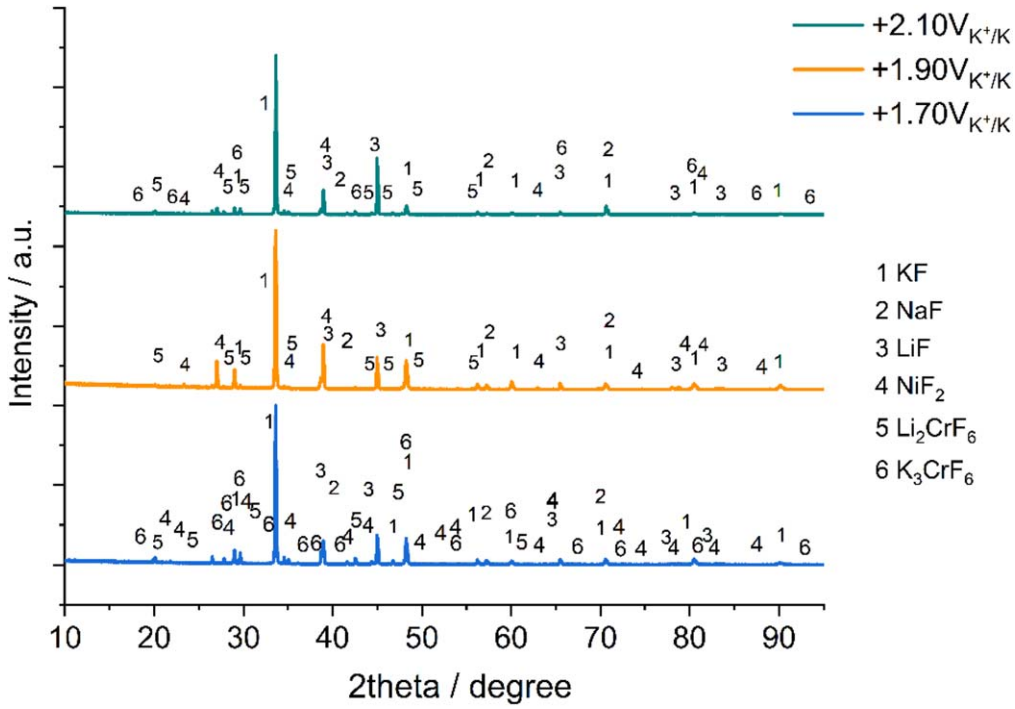

Figure 10. X-ray diffractogram of as-solidified salt mixture subjected to Ni20Cr potentiostatic hold at (a) +1.75 $V_{K+/K}$, (b) +1.90 $V_{K+/K}$, and (c) +2.10 $V_{K+/K}$ in FLiNaK, 600 °C for 10 ks.

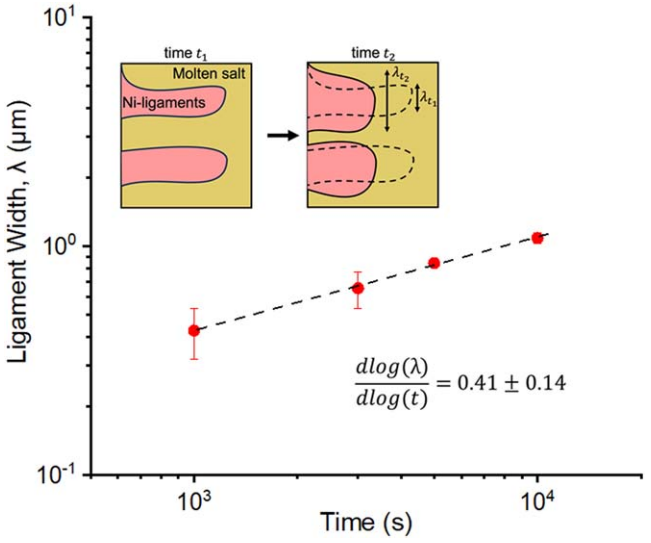

Figure 11. Plan view measurements of ligament width between 1 and 10 ks for Ni20Cr (wt%) potentiostatically polarized in Molten FLiNaK at 600 °C. The inset displays a simplified schematic of Ni-rich ligament coarsening process.

Table II. Correlation Between Potentiostatic Hold Potential, Total Charge Consumed, and Select Microstructural Properties in Ni20Cr (wt.%) Alloys post 10ks of potentiostatically dealloying in Molten FLiNaK FLiNaK at 600 °C.

E (vs K^+/K)	$h_{dissolved}$ (μm)	w (μm)	λ (μm)
1.75	1.09	0.81 ± 0.18	0.29 ± 0.08
1.90	12.2	10.9 ± 3.45	0.95 ± 0.15
2.10	44.9	12.0 ± 2.83	8.99 ± 1.37

Table III. Plan View Measurements of Ligament Width for Ni20Cr potentiostatically polarized at +1.90 $V_{K+/K}$ for 1, 3, 5 and 10 ks in Molten FLiNaK at 600 °C.

Time (ks)	λ (μm)
1	0.43 ± 0.11
3	0.65 ± 0.12
5	0.84 ± 0.14
10	1.08 ± 0.26

$$\frac{d\lambda^n}{dt} = \text{constant} \quad [7]$$

where n is a coarsening exponent, and t is time. In this work, we chose the feature size to be the ligament width measured in plane view based on Fig. 7, since these ligaments will have already undergone dealloying and their evolution is only governed by coarsening and capillary effects. It is noted that a n value of 4 corresponds to a coarsening process that is a surface diffusion mediated process, whereas a value of 3 indicates bulk diffusion mediated.[66–69]

As shown in Fig. 11 and Table III, the ligament width and time display a slope of 0.41 ± 0.14 μm, which corresponds to a n value of 2.43 ± 1.26. Therefore, the current data cannot conclusively determine whether coarsening behavior is dominated solely by surface or bulk diffusion. Nevertheless, the measurement is carried out on the plane view of a limited size of dealloying times while the ligament size may possibly vary with the dealloying depth,[16] suggesting the need for further study to confirm these findings. When ligament coarsening is primarily controlled by Ni surface diffusion and capillary forces for the minimization of surface free energy, the surface diffusivity of Ni (D_s^{Ni}) may be estimated via Eq. 8:[70–72]

$$D_s^{Ni} = \frac{\lambda^4 kT}{32\gamma t a^4} \quad [8]$$

where k is the Boltzmann constant ($1.38{\cdot}10^{-23}$ J K^{-1}), γ is surface energy of Ni in molten salts (an assumed value of 200 mJ m^{-2} due to the lack of experimental and computational data related to the interface between metal and molten salt),[70] t is the potentiostatic polarization hold time, T is temperature, and a is the lattice parameter of pure Ni at 600 °C (a value of 0.356 nm was used).[73] The estimation of surface energy is based on the findings presented by Marcus et al.[74] Equation 8 is only used for the condition of +1.75 $V_{K+/K}$ and +1.90 $V_{K+/K}$ since significant Ni dissolution is seen at +2.10 $V_{K+/K}$ and this effect cannot be ignored. This yields D_s^{Ni} values of $8.02{\cdot}10^{-10}$ and $9.93{\cdot}10^{-8}$ cm^2 s^{-1}, which are at least three orders of magnitude higher than the typical range of D_s^{Ni} reported in room temperature aqueous solution between 10^{-13} and 10^{-16} cm^2 s^{-1}.[66,75] This increase is expected at the elevated temperatures for FLiNaK and is thermally activated. Furthermore, the curvature induced by the ligaments (i.e., convex ligaments and concave pores) also drives the further coarsening and densification behavior as reported by Henkelmen et al.[76] Their experimental observations and kMC simulations bear a striking resemblance to those depicted in Figs. 4, 6, and 9.

Using the nominal diffusion equation ($x = \sqrt{Dt}$), the calculation shows that in 10 ks at 600 °C and $T_H = 0.522$, surface diffusion of unoxidized Ni can readily occur across distances exceeding 1 μm (1000 nm). This likely contributes to the reorganization of Ni into new FCC ligament structures, potentially realigning their orientations to alleviate stress. Additionally, it is acknowledged that the rapid Ni surface diffusion may potentially decelerate both interfacial Cr dissolution ($J_{electric}$) and bulk transport of Cr (J_{Bulk}^{Cr}) as it alters the alloy surface chemistry and microstructure. However, determining the extent of this effect necessitates more sensitivity analysis in our future study.

The following presents a hypothesis to explain the apparent Ni ligament coarsening behavior with applied potential. Based on the Terrace-Ledge-Kink model (TLK)[77] and the Gibbs-Thomson effect, as dealloying occurs Ni adatoms can surface-diffuse to passivate receding sites created by Cr dissolution, which include step edges, terrace, and kink sites.[52,78–80] As the electrode potential approaches the Ni dissolution potential, the diffusion rates of kink sites can increase drastically—an observation made by Kolb et al. using scanning tunneling microscope during potentiostatic dealloying of Ag-Au.[63] This behavior was attributed to the interaction between possible physi-/chemi-absorbed species and the double layer.[63–65] When the dissolution of Ni becomes favorable, two phenomena may occur: (1) structures formed by surface reconstruction may be annihilated and lowering the energy barriers for surface diffusion;[63–65,81] (2) Ni adatoms preferentially dissolve due to their low-coordination nature,[78] leaving Ni atoms situated in the more coordinated step edges or terrace sites to passivate vacancies created by Cr dissolution. Either mechanism is a function of crystallographic orientation. Higher index, more irrational planes exhibit a different or lower γ (thus a higher D_s from Eq. 8), shorter hopping distance, higher number of low-coordination sites,[78] and possibly leads to faster ligament coarsening. Consequently, despite all three applied potentials having identical potentiostatic polarization periods, the Ni ligaments are coarser at high potentials possibly due to an enhanced MN surface mobility.

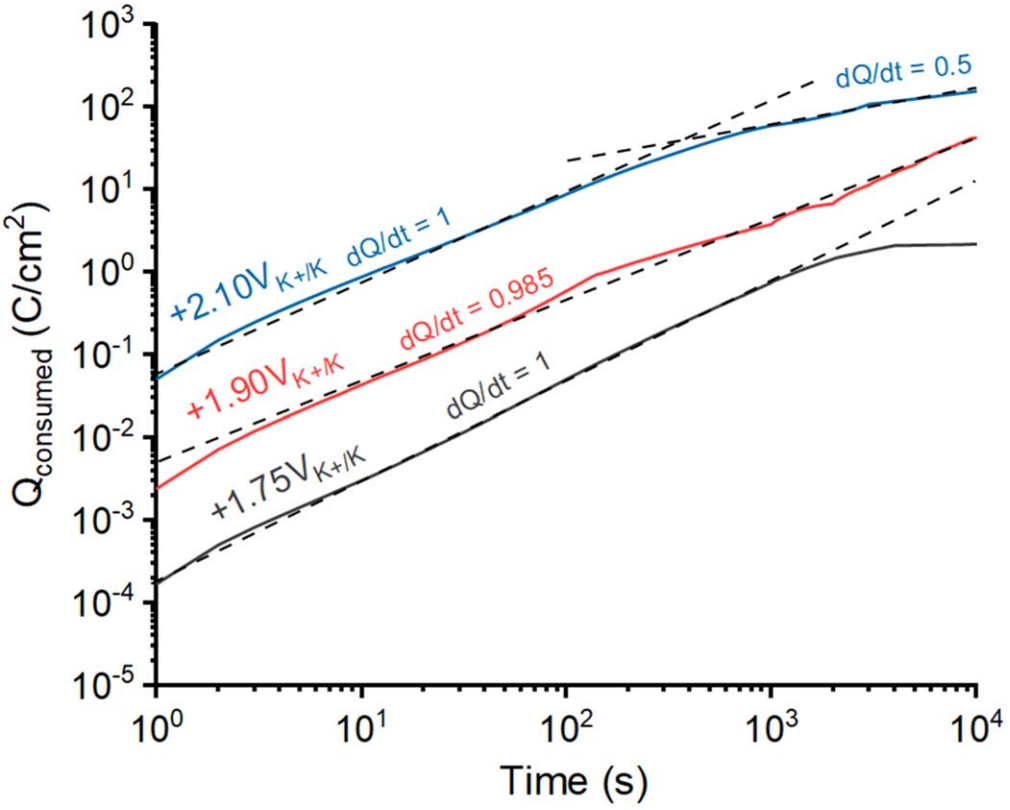

Figure 12. Cumulative charge ($Q_{consumed}$) during the potentiostatic hold of Ni20Cr in molten FLiNaK salts, 600 °C at +1.75 $V_{K+/K}$, +1.90 $V_{K+/K}$, and +2.10 $V_{K+/K}$ for 10 ks.

Applied potential effect on electrolytic dissolution.—In aqueous dealloying studies, the potentiostatic polarization method (also known as chronoamperometry) is a popular approach for fabricating bicontinuous dealloying porous structures, particularly in Ag-Au systems.[28,34,75,82] The trend of current decay over time, i.e. $i \propto t^{-n}$, can also shed light on possible rate-controlling surface diffusion mechanisms, as further elucidated by Sieradzki et al.[53,82] However, these relationships are not as apparent in molten salt systems. Depending on the applied potentials (such as +1.90 $V_{K+/K}$), the anodic current behavior could remain at a relatively constant magnitude over time. Such behavior has also been noted in molten chlorides[19] and fluorides[25] systems. This may be explained by the recent kMC modeling by Henkelmann et al.,[76] who simulated the i-t behavior for surface-mediated primary and secondary dealloying behavior on a nanoporous gold alloy.

Figure 12 illustrates that $Q_{consumed}\left(=\int_0^t i\,dt\right)$ increases linearly with increasing time at fixed i, exhibiting a unity slope and suggesting CT- controlled behavior. For the +1.75 V_{K+K} condition, the plateau of the curve can be attributed to the net current density dropping to near zero as $i_{electric}$ switches to cathodic. A unity slope suggests that the reaction proceeds at a consistent rate, with both the dissolution rate and the outward diffusing supply of receding Cr and/or Ni remaining steady. Intriguingly, at +2.10 V_{K+K}, the slope shifts to 0.5 starting at 409 s, as highlighted by the black arrow. A slope of 0.5 points to potential mass transport limitations.[83] These could arise from bulk Cr lattice diffusion and/or possibly from limitations in the longer range, ionic phase mass transport away from the salt metal interface due to salt film formation on corrosion pores (Fig. S8).[17] This observation is consistent with the R_{ct} trend (which is inversely proportional to the interfacial dissolution rate[84]) with time extracted from EEC fittings of EIS spectra as displayed in Fig. 13 and Table S6. Both the +1.75 V_{K+K} and +1.90 V_{K+K} conditions exhibit relatively constant R_{ct} values. However, the +2.10 V_{K+K} condition

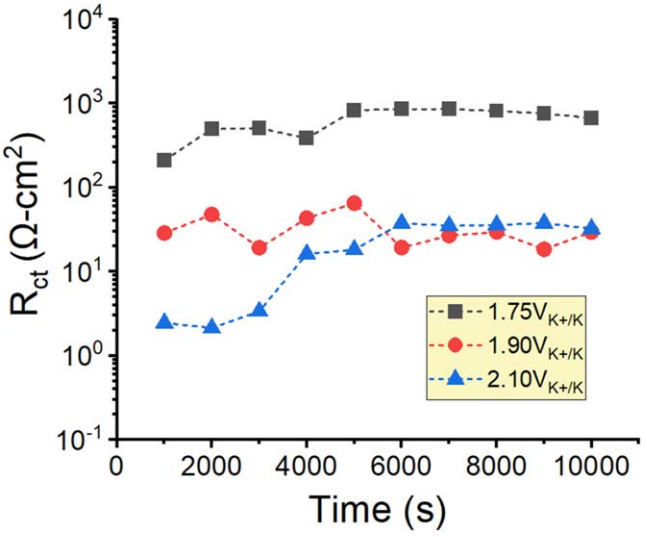

Figure 13. Charge transfer resistance (R_{ct}) of Ni20Cr (wt.%) in molten FLiNaK salts, 600 °C potentiostatically held at +1.75 $V_{K+/K}$, +1.90 $V_{K+/K}$, and +2.10 $V_{K+/K}$ for 10 ks.

reveals an order of magnitude decrease in R_{ct}, coinciding where the rate of dissolution is MT-limited through the salt film.

Effect of bulk diffusion on dealloying.—We now shift our focus to the transport of Cr in the Ni20Cr alloy. EDS line scans reveal that Cr, being the LN element, is retained at the ~5 wt% level within the surface ligaments at +1.75 $V_{K+/K}$. However, at higher potentials of +1.90 $V_{K+/K}$ and +2.10 $V_{K+/K}$, Cr is completely depleted from both the ligaments and the dealloyed zone (Figs. 6 and 9). This partial depletion raises questions about the necessity of Ni reorganizing into

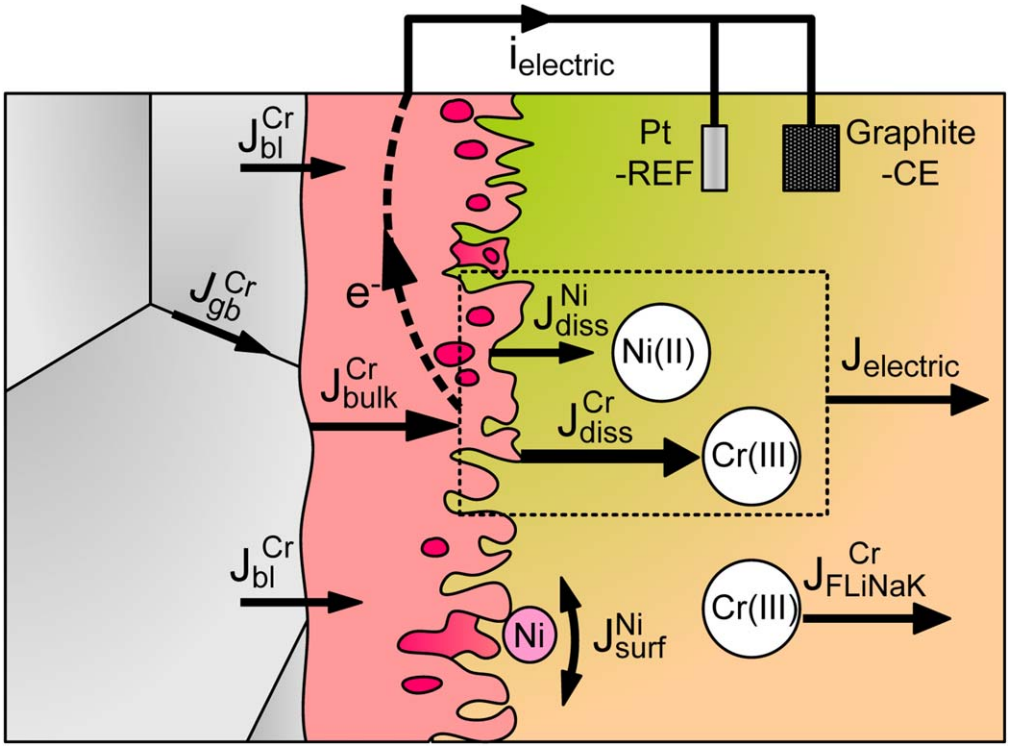

Figure 14. Schematics displaying a simplified mechanism of molten fluoride dealloying.

new grains with various crystallographic orientations. At higher T_H, the bulk diffusion of Cr, via lattice and short-circuit pathways, can become predominant.[15,32] A standing question is whether the bulk diffusion of Cr can sufficiently maintain the $J_{electric}$—the interfacial dissolution rate measured. The following consideration assumes only Cr oxidation is the source of anodic charge that is solely responsible for $J_{electric}$. By equating the necessary $J_{electric}$ to a hypothetical Cr bulk diffusion flux, represented as J^{Cr}_{Bulk}, the required J^{Cr}_{Bulk} to match $J_{electric}$ can be described as a function of $i_{electric}$ using Eq. 9:

$$J_{electric} = J^{Cr}_{Bulk} = \frac{i_{electric}}{zF} \quad [9]$$

where z represents the oxidation state of the dissolved species (assumed to be 3). The $i_{electric}$ values are measured at each dealloying potential (Figs. 3, 5, 8). At constant $J_{electric}$, the solid-state bulk Cr diffusion flux (J^{Cr}_{Bulk}) can be estimated with Fick's 1st Law assuming a pseudo-steady state diffusion condition, starting with Eq. 10:

$$J^{Cr}_{Bulk} = -D^{Cr}_{eff}\frac{\Delta C^{Cr}}{\Delta x} \quad [10]$$

where Δx is the diffusion distance and ΔC^{Cr} is the difference between bulk and depleted concentrations of Cr as a result of the selective leaching of Cr from the alloy. The ΔC_{Cr} value is taken to be 0.0340 mol cm^{-3} (equivalent to complete Cr depletion). Accordingly, the effective solid-state diffusion coefficient (D^{Cr}_{eff}) for Cr in FCC Ni20Cr including grain boundaries can be quantitatively assessed using Eq. 11:

$$D^{Cr}_{eff} = \left(\frac{2\delta}{L}\right)D^{Cr}_{gb} + \left(1 - \frac{2\delta}{L}\right)D^{Cr}_{l} \quad [11]$$

where D_{gb} and D_l are the grain boundary and bulk diffusivities of Cr in Ni20Cr in cm^2/s, δ is the grain boundary thickness ($\sim 10^{-7}$ cm[85]), and L is the grain size. Based on published literature, the D_{gb} and D_l of Cr in Ni20Cr are on the order of $9.55{\cdot}10^{-11}$ cm^2/s and $8.71{\cdot}10^{-15}$ cm^3/s at 600 °C, respectively.[86–89] With an average L of 351 μm (Fig. S1), the D_{eff} for Cr diffusion is taken as $9.25{\cdot}10^{-15}$ cm^2/s. Equation 11 does not consider the effects of non-equilibrium vacancies nor dislocations that may also accelerate solid-state diffusion. It is important to note that J^{Cr}_{Bulk} is also time-dependent. To connect J^{Cr}_{Bulk} with time (Δt), Δx is estimated using the nominal diffusion distance via Eq. 12:

$$\Delta x = \sqrt{D^{Cr}_{eff}\Delta t} \quad [12]$$

Rearranging Eqs. 10 and 12 results in Eq. 13, which is the time-dependent current density ($i^{required}_{electric}$) corresponding to a condition where Cr bulk diffusion becomes the rate-limiting mechanism in a series of diffusion processes (see Fig. 14).

$$J^{Cr}_{Bulk} = -\frac{\Delta C^{Cr}\sqrt{D^{Cr}_{eff}}}{\sqrt{\Delta t}} \quad [13]$$

Moreover, to compare with the possible mass-transport effect in the ionic phase, the diffusion flux of Cr (III) ions in FLiNaK can also be estimated using Eq. 14:

$$J^{Cr(III)}_{FLiNaK} = \frac{D_{Cr}C_{Cr(III)}}{\delta_b} \quad [14]$$

where $D^{Cr(III)}_{FLiNaK}$ is the diffusivity of Cr (III) ions in FLiNaK at 600 °C (assumed to be 10^{-5} cm^2/s[10,25]), δ_b is the boundary layer thickness (estimated to be 10 μm[25]), and $C_{Cr(III)}$ is the concentration of dissolved Cr in mol/cm^3. Equation 15 can also be expressed as a function of time:

$$J^{Cr(III)}_{FLiNaK} = \frac{C_{Cr(III)}\sqrt{D^{Cr(III)}_{FLiNaK}}}{\sqrt{\Delta t}} \quad [15]$$

The Faraday's law of mass and charge conversion, akin to Eq. 5, can be used to calculate $C_{Cr(III)}$, resulting in Eq. 16:

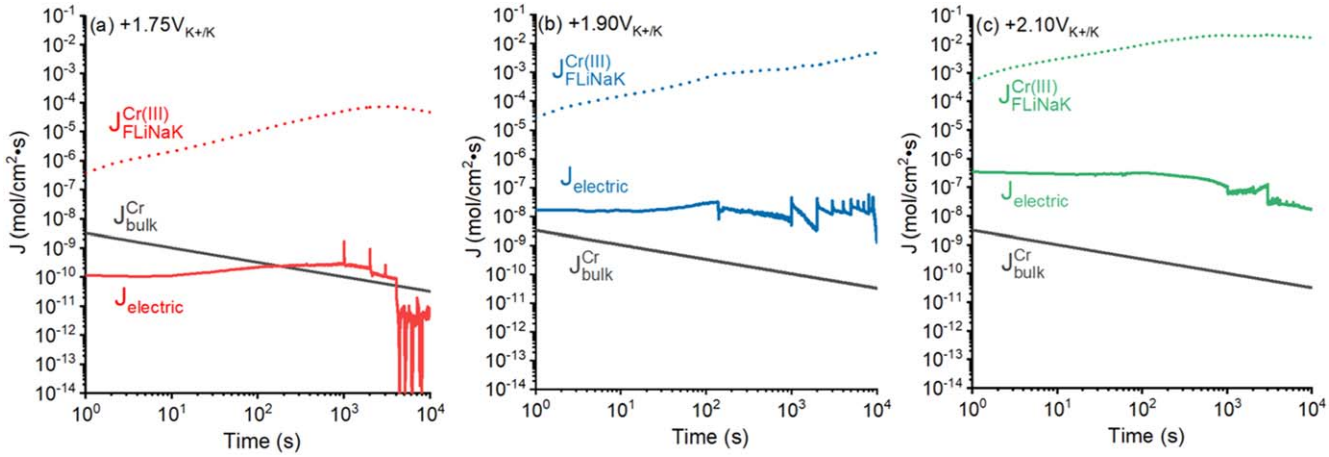

Figure 15. Dissolution flux ($J_{electric}$) vs time for Ni20Cr (wt%) potentiostatically held at (a) +1.75 $V_{K+/K,}$ (b) +1.90 $V_{K+/K}$, and (c) +2.10 $V_{K+/K}$ for 10 ks. The solid grey line represents the calculated effective bulk diffusion flux (J^{Cr}_{Bulk}) and the dashed line shows the ionic diffusion flux of Cr(III), $J^{Cr}_{FLiNaK,}$ ions in FLiNaK at 600 °C.

$$J^{Cr(III)}_{FLiNaK} = \frac{EW * Q_{consumed} * \sqrt{D^{Cr(III)}_{FLiNaK}}}{V_{FLiNaK}\sqrt{\Delta t}} \quad [16]$$

where V_{FLiNaK} is 15 cm^3 representing the volume of FLiNaK salt used in this study. J^{Cr}_{FLiNaK} is calculated for each dealloying potential condition. Figure 14 presents a simplified schematic of the multiple diffusion processes that occur concurrently during molten salt dealloying.

Figure 15 presents a comparative analysis of $J_{electric}$, J^{Cr}_{Bulk}, and $J^{Cr(III)}_{FLiNaK}$ over time. At +1.75 $V_{K+/K}$, J^{Cr}_{Bulk} at first exceeds $J_{electric}$ for the initial ~200 s of the potentiostatic hold period, suggesting that the bulk diffusion of Cr is sufficiently fast to support the Cr dissolution reaction, but not for extended periods of time. This can lead to significant salt penetration by dealloying to develop the observed corrosion pores. As time progresses and $J_{electric}$ exceeds J^{Cr}_{Bulk}, $J_{electric}$ decreases slightly and diminishes to nearly zero as Cr is only supplied when Ni surface diffusion uncovers unexposed FCC Ni-Cr. Moreover, for the entire 10 ks hold period, $J^{Cr(III)}_{FLiNaK}$ is at least three orders of magnitude larger than $J_{electric}$ and J^{Cr}_{Bulk}, and thus ionic diffusion of Cr(III) is unlikely to act as a rate-limiting step in the process at any potential. This observation holds true for the dealloying potentials of +1.75 (Fig. 14a), +1.90 $V_{K+/K}$ (Fig. 14b) and +2.10 $V_{K+/K}$ (Fig. 14c).

On the contrary, $J_{electric}$ is higher than J^{Cr}_{Bulk} for the entire potentiostatic hold period for +1.90 $V_{K+/K}$ and +2.10 $V_{K+/K}$. This suggests that the dealloying process at constant potential can be rate-limited by the insufficient bulk transport of Cr. At potentials higher than +2.10 $V_{K+/K}$, the dissolution of Cr to Cr(III) and Ni to Ni(II) is relatively fast. The combination of insufficient bulk outward diffusion of Cr and an expected increase in J^{Ni}_{diss} causes the uniform dissolution rate to exceed the dealloying rate at these high potentials. At some potential both the rate of LN and MN dissolution results in a smooth surface morphology. Here, the uniform corrosion front moves at a velocity exceeding the dealloying front. It is noted that J^{Cr}_{Bulk} can be increased by increasing temperature,[20] reducing grain sizes,[27] cold working,[26] radiating the alloy,[31] or any other means to introduce defects to the alloys.[2]

The interaction between the interfacial dealloying process, the underlying microstructure, and how the role of crystallographic orientation to modify the rates and mechanisms by which surface diffusion and bulk-diffusion controlled dealloying are all current subjects of investigation. The findings of this current study provides a foundational methodology and dealloying condition that will allow us to interrogate and isolate these individual effects. Another open knowledge gap is the speciation effect of metallic cations in molten salts, e.g. CrF_6^{3-} in molten fluorides,[6,9,90] on the development of dealloying structure. For instance, speciation can modify the driving force of LN dissolution (thus altering $J_{electric}$),[6,9] alter the surface mobilities of MN,[91] possibly restrict the refinement of pore size due to the larger ionic radii,[52,92,93] and/or slow down the long-range diffusion of corrosion products in molten salts.[18] Lastly, independent *in-operando* elemental measurements (in the liquid salt) have not been conducted and may be the subject of future studies.

Conclusions

This work investigates the morphologiacl evolution of Ni20Cr (wt.%) in FLiNaK at 600 °C at a systematic range of applied potentials between +1.75 $V_{K+/K}$ and 2.75 $V_{K+/K}$. By employing a framework that couples thermo-kinetic analysis and *in-operando* electrochemistry, with a multi-modal materials characterization methods to enable the pinpointing of rate-limiting mass transport mechanisms at different potential regimes in molten eutectic LiF-NaF-KF salt. At an intermediate potential regime between +1.75$V_{K+/K}$ and +2.10$V_{K+/K}$ for 10ks at high homologous temperature, bicontinuous dealloying is evident through the formation of a micron-scale interconnected pure Ni ligament-pores network. Only Cr dissolved at +1.75 $V_{K+/K}$. With increasing applied potential, there is a noticeable bulk diffusion-assisted coarsening and densification of the Ni ligaments.

In this regime, the bulk outward diffusion of Cr (J^{Cr}_{bulk}) initially exceeds the dissolution flux ($J_{electric}$) at +1.75$V_{K+/K,}$ but subsequently falls below $J_{electric}$, suggesting Cr bulk outward diffusion eventually limits the dealloying process. At the metal/salt interface under CT controlled dissolution, Cr is instantly oxidized. At the higher potentials of +1.90$V_{K+/K}$ and +2.10$V_{K+/K,}$ $J_{electric}$ consistently surpasses J^{Cr}_{bulk} from the outset, signaling that J^{Cr}_{bulk} is not sufficient to sustain the dissolution reactions of Cr and Ni. Under these conditions, the dissolution of Ni also contributes to $J_{electric}$. The ionic phase Cr(III) ion diffusion in FLiNaK is not rate-limiting at these potentials. Therefore, it is evident that while the impact of the Cr bulk is significant in the context of molten salt dealloying, the rate-limiting step can shift depending on the applied potential and the duration of the process. The applied potential (or driving force) determines the dissolution rates of Cr and Ni, while time reflects the morphological evolution that affects J^{Cr}_{bulk}.

At the elevated potential regime between +2.30 $V_{K+/K}$ and +2.50 $V_{K+/K}$, mixed CT- and MT-controlled dissolution of both Cr and Ni lead to the formation of a crystallographic faceted structure.

At high enough potential, the rate of Ni(II) release is nearly as fast as that of Cr(III) and evidence of dealloying disappears as uniform dissolution occurs at nearly the same rate as dealloying. Hence the dissolution flux of surface Ni (J^{Ni}_{diss}) also becomes significant. At +2.75 $V_{K+/K}$, electro-dissolution is completely regulated by MT-controlled behavior due to the formation of a potentially K-Cr-Ni-F salt film, leading to the smoothing of surfaces. At this potential, Ni (II) and Cr(III) are dissolving at nearly the same rate. The presence of the salt film can also be observed on the edges of corrosion pores at the dealloying potential of +2.10 $V_{K+/K}$. This suggests an additional mass transport constraint arising from the diffusion of corrosion products, such as Cr(III) and Ni(II), through salt-penetrated channels.

These analyses point to the bulk outward diffusion of LN(Cr) as the predominant mechanism driving molten salt dealloying at high homologous temperatures. The occurrence of bicontinuous dealloying necessitates specific combinations of $J_{electric}$, J^{Cr}_{bl}, J^{Cr}_{gb}, J^{Ni}_{diss}, and J^{Ni}_{surf}. Bicontinuous morphologies still forms when Ni dissolves at +1.90$V_{K+/K}$ and +2.10$V_{K+/K}$, likely due to the J^{Ni}_{diss} being sufficiently low relative to J^{Cr}_{diss} and J^{Ni}_{diff}. The current findings suggest that the interplay of rapid bulk diffusion, surface diffusion, and interfacial dissolution of Cr and Ni, underlined by a constant current may enable fast dealloying in a specific potential range.

Acknowledgments

This work was supported as part of FUTURE (Fundamental Understanding of Transport Under Reactor Extremes), an Energy Frontier Research Center funded by the U.S. Department of Energy, Office of Science, Basic Energy Sciences. H.C. acknowledges the National Science Foundation Graduate Research Fellowship Program (NSF GRFP) grant no. 1842490. HDTEM work was conducted at the Molecular Foundry and was supported by the Office of Science, Office of Basic Energy Sciences, of the U.S. Department of Energy under Contract No. DE-AC02–05CH11231.

ORCID

Ho Lun Chan https://orcid.org/0000-0001-5257-2551
Elena Romanovskaia https://orcid.org/0000-0001-8815-356X
Valentin Romanovski https://orcid.org/0000-0003-1741-0316
John R. Scully https://orcid.org/0000-0001-5353-766X

References

1. D. Rodrigues et al., *Nukleonika*, **60**, 907 (2015).
2. S. Guo et al., *Prog. Mater Sci.*, **97**, 448 (2018).
3. F. Schmidt et al., *Annu. Rev. Mater. Res.*, **51**, 293 (2021).
4. H. E. McCoy and R. E. Gehlbach, *Nucl. Technol.*, **11**, 45 (1971).
5. R. Auguste et al., *npj Mater Degrad*, **6**, 113 (2022).
6. H. L. Chan et al., *npj Mater Degrad*, **6**, 46 (2022).
7. E. Romanovskaia et al., *Corros. Sci.*, **222**, 111389 (2023).
8. S. S. Raiman and S. Lee, *J. Nucl. Mater.*, **511**, 523 (2018).
9. H. L. Chan and J. R. Scully, *Corrosion*, **79**, 1236 (2023).
10. Y. Wang and J. Zhang, *J. Electrochem. Soc.*, **167**, 086503 (2020).
11. K. K. Sandhi and J. Szpunar, *Energies*, **14**, 543 (2021).
12. L. C. Olson et al., *J. Fluorine Chem.*, **130**, 67 (2009).
13. Y. L. Wang et al., *Corros. Sci.*, **103**, 268 (2016).
14. F.-Y. Ouyang et al., *J. Nucl. Mater.*, **437**, 201 (2013).
15. T. Ghaznavi et al., *J. Electrochem. Soc.*, **169**, 111506 (2022).
16. K. Bawane et al., *Corros. Sci.*, **195**, 109962 (2022).
17. X. Liu et al., *Nat. Commun.*, **12**, 3441 (2021).
18. L.-C. Yu et al., *Sci Rep.*, **12**, 20785 (2022).
19. T. Ghaznavi et al., *J. Electrochem. Soc.*, **169**, 061502 (2022).
20. T. Ghaznavi et al., *Corros. Sci.*, **197**, 110003 (2022).
21. H. Gholamzadeh et al., *Acta Mater.*, **260**, 119278 (2023).
22. *Electrochemical Impedance: Analysis and Interpretation*J. R. Scully, D. C. Silverman, and M. W. Kendig et al. (ed.), (ASTM STP 1188, Philadelphia) 94 (1993).
23. R. N. Wright and T.-L. Sham, *Status of Metallic Structural Materials for Molten Salt Reactors INL/EXT-18-45171*, Idaho National Laboratory, (2018).
24. N. Bieberdorf et al., *NPJ Comput. Mater.*, **9**, 127 (2023).
25. H. L. Chan et al., *J. Electrochem. Soc.*, **170**, 081502 (2023).
26. M. Maric et al., *Corros. Sci.*, **142**, 133 (2018).
27. Y. L. Wang et al., *Corros. Sci.*, **109**, 43 (2016).
28. D. M. Artymowicz et al., *Philos. Mag.*, **89**, 1663 (2009).
29. H. L. Chan et al., *Materialia*, **28**, 101762 (2023).
30. Y. Q. Yang et al., *Corros. Sci.*, **204**, 110381 (2022).
31. W. Zhou et al., *Nat. Commun.*, **11**, 3430 (2020).
32. X. Liu et al., *ACS Appl. Mater. Interfaces*, **15**, 13772 (2023).
33. A. Ronne et al., *ACS Appl. Mater. Interfaces*, **12**, 17321 (2020).
34. D. Artymowicz, R. Newman, and J. Erlebacher, *ECS Trans.*, **3**, 499 (2007).
35. R. H. Banerjee et al., *Corros. Sci.*, **212**, 110929 (2023).
36. J. Erlebacher et al., *Nature*, **410**, 450 (2001).
37. Y. Li et al., *Acta Mater.*, **222**, 117424 (2022).
38. G. Zheng and K. Sridharan, *JOM*, **70**, 1535 (2018).
39. D. Sulejmanovic et al., *J. Nucl. Mater.*, **553**, 152972 (2021).
40. L. Olson et al., *J. Nucl. Mater.*, **411**, 51 (2011).
41. W. H. Doniger et al., *J. Electrochem. Soc.*, **169**, 071502 (2022).
42. L. Massot, M. Gibilaro, D. Quaranta, and P. Chamelot, *J. Electrochem. Soc.*, **168**, 026510 (2021).
43. J. Qiu et al., *Corros. Sci.*, **186**, 109457 (2021).
44. R. Kelly, J. Scully, D. Shoesmith, and R. Buchheit, *Electrochemical Techniques in Corrosion Science and Engineering* (CRC Press, Boca Raton, FL) (2002), (https://taylorfrancis.com/books/9780203909133).
45. ASTM International, *Standard Practice for Calculation of Corrosion Rates and Related Information from Electrochemical Measurements ASTM G102-89*, ASTM International (2015), 03.
46. H. Yin et al., *J. Fluorine Chem.*, **209**, 6 (2018).
47. N. D. Smith et al., *J. Electrochem. Soc.*, **170**, 066505 (2023).
48. S. Fabre et al., *J. Nucl. Mater.*, **441**, 583 (2013).
49. J. A. Ocadiz-Flores et al., *The Journal of Chemical Thermodynamics*, **121**, 17 (2018).
50. J. Ge et al., *J. Phys. Chem. B*, **127**, 8669 (2023).
51. I. McCue et al., *Acta Mater.*, **115**, 10 (2016).
52. I. McCue et al., *Annu. Rev. Mater. Res.*, **46** (2016).
53. K. Sieradzki et al., *J. Electrochem. Soc.*, **134**, 1635 (1987).
54. H. W. Pickering, *Corros. Sci.*, **23**, 1107 (1983).
55. R.-D. Grimm and D. Landolt, *Corros. Sci.*, **36**, 1847 (1994).
56. V. Pavlík et al., *New J. Chem.*, **39**, 9841 (2015).
57. H. Yin et al., *Corros. Sci.*, **131**, 355 (2018).
58. M. Hong et al., *Corros. Sci.*, **212**, 110913 (2023).
59. R. B. Evans III, J. H. Devan, and G. M. Watson, *Self-Diffusion of Chromium In Nickel-Base Alloys. ORNL-2982*, Oak Ridge National Laboratory (1961).
60. M. C. van Ede and U. Angst, *Corrosion*, **78**, 1087 (2022).
61. P. Jakupi, D. Zagidulin, J. J. Noël, and D. W. Shoesmith, *Electrochim. Acta*, **56**, 6251 (2011).
62. T. Dumaire, R. J.-M. Konings, and A. L. Smith, *Thermo*, **1**, 205 (2021).
63. D. M. Kolb, G. Lehmpfuhl, and M. S. Zei, *Spectroscopic and Diffraction Techniques in Interfacial Electrochemistry*, 361 (1990).
64. D. Kolb, *Prog. Surf. Sci.*, **51**, 109 (1996).
65. D. M. Kolb and J. Schneider, *Electrochim. Acta*, **31**, 929 (1986).
66. S. A. Policastro et al., *J. Electrochem. Soc.*, **157**, C328 (2010).
67. W. W. Mullins, *J. Appl. Phys.*, **30**, 77 (2004).
68. Y. K. Chen-Wiegart et al., *Acta Mater.*, **60**, 4972 (2012).
69. J. Erlebacher, *Phys. Rev. Lett.*, **106**, 225504 (2011).
70. C. Alonso et al., *J. Electrochem. Soc.*, **137**, 2161 (1990).
71. L. H. Qian and M. W. Chen, *Appl. Phys. Lett.*, **91**, 083105 (2007).
72. R. Song et al., *Nat. Commun.*, **13**, 5157 (2022).
73. J. Zhang and P. A. Korzhavyi, *Metals*, **10**, 319 (2020).
74. Y. Marcus, *Thermochim. Acta*, **571**, 77 (2013).
75. A. Dursun et al., *J. Electrochem. Soc.*, **150**, B355 (2003).
76. G. Henkelmann et al., *Nano Lett.*, **22**, 6787 (2022).
77. B. E. Douglas and S.-M. Ho, *Structure and Chemistry of Crystalline Solids. Structure and Chemistry of Crystalline Solids* (Springer, New York) (2006).
78. J. Erlebacher, *J. Electrochem. Soc.*, **151**, C614 (2004).
79. J. Erlebacher and R. Seshadri, *MRS Bull.*, **34** (2009).
80. J. Erlebacher and K. Sieradzki, *Scr. Mater.*, **49**, 991 (2003).
81. J. Xu et al., *J. Phys. Chem. C*, **116**, 5689 (2012).
82. K. Wagner et al., *J. Electrochem. Soc.*, **144**, 3545 (1997).
83. D. M. Rishel et al., *Mater. Sci. Eng. A*, **143**, 197 (1991).
84. J. R. Scully, *Corrosion*, **56**, 199 (2000).
85. J. Ding et al., *Nanoscale*, **11**, 23449 (2019).
86. T.-F. Chen et al., *Mater. Trans.*, **44**, 40 (2003).
87. S. P. Murarka et al., *J. Appl. Phys.*, **35**, 1339 (1964).
88. "T. Ghenoet al." *Materialia*, **3**, 145 (2018).
89. T.-F. Chen et al., *J. Nucl. Mater.*, **169**, 285 (1989).
90. N. Winner et al., *J. Mol. Liq.*, **335**, 116351 (2021).
91. R. O'Hare, *Materials Kinetics Fundamentals* (Wiley, New Jersey) (2015).
92. C. Bessada et al., *in Molten Salts Chemistry and Technology* (John Wiley & Sons, Ltd.) 219 (2014).
93. Q. Jie et al., *Nucl. Sci. Tech.*, **26**, 060602 (2015).